2005

Optical Identification of Infrared Space Observatory Far-Infrared Sources in the Lockman Hole Using a Deep Very Large Array 1.4 GHz Continuum Survey

S Oyabu

Min Yun
University of Massachusetts - Amherst

T Murayama

DB Sanders

K Kawara

See next page for additional authors

Recommended Citation

Oyabu, S; Yun, Min; Murayama, T; Sanders, DB; Kawara, K; Taniguchi, Y; Veilleux, S; Okuda, H; Matsuhara, H; Cowie, LL; Sato, Y; Wakamatsu, K; and Sofue, Y, "Optical Identification of Infrared Space Observatory Far-Infrared Sources in the Lockman Hole Using a Deep Very Large Array 1.4 GHz Continuum Survey" (2005). *The Astrophysical Journal*. 1127.
https://doi.org/10.1086/462420

Optical identification of ISO far-infrared sources in the Lockman Hole using a deep VLA 1.4 GHz continuum survey

S. Oyabu[1,2,*], Min S. Yun[2,3], T. Murayama[4], D.B. Sanders[5], K. Kawara[1], Y. Taniguchi[4], S. Veilleux[6], H. Okuda[7,8], H. Matsuhara[7], L.L. Cowie[5], Y. Sato[2,9], K. Wakamatsu[10]

and

Y. Sofue[1]

oyabu@ir.isas.jaxa.jp

ABSTRACT

By exploiting the far-infrared(FIR) and radio correlation, we have performed the Likelihood-Ratio analysis to identify optical counterparts to the far-infrared sources that have been found in an area of ~ 0.9 deg^2 during the ISO deep far-infrared survey in the Lockman Hole. New ground-based observations have been conducted to build up the catalogs of radio and optical objects, which include a deep VLA observation at 1.4 GHz, optical $R-$ & I-band imaging on the Subaru 8m and UH 2.2m telescopes, and optical spectroscopy on the Keck II 10m and WIYN 3.5m telescopes. This work is based on the FIR sample consisting of 116 and 20 sources that are selected with the criteria of $F^C(90\mu\mathrm{m}) \geq 43$ mJy or $F^C(170\mu\mathrm{m}) \geq 102$ mJy, respectively, where F^C is

[1]Institute of Astronomy, the University of Tokyo, 2-21-1, Osawa, Mitaka, Tokyo, 181-0015, Japan

[2]Visiting Astronomer, WIYN, National Optical Astronomy Observatory, which is operated by the Association of Observatories for Research in Astronomy, Inc. (AURA) under cooperative agreement with the National Science Foundation.

[3]Department of Astronomy, University of Massachusetts, 619 Lederle Graduate Research Center, Amherst, MA 01003

[4]Astronomical Institute, Tohoku University, Aoba, Sendai 980-77, Japan

[5]Institute for Astronomy, University of Hawaii, 2680 Woodlawn Drive, Honolulu, HI 96822, USA

[6]Department of Astronomy, University of Maryland, College Park, MD 20742

[7]Institute of Space and Astronautical Science, Japan Aerospace Exploration Agency, 3-1-1 Yoshinodai, Sagamihara, Kanagawa, 229-8510, Japan

[8]Gunma Astronomical Observatory, Gunma 377-0702, Japan

[9]National Astronomical Observatory of Japan, Mitaka, Tokyo 181-8588, Japan

[10]Faculty of Engineering, Gifu University, Gifu 501-1193, Japan

[*]Present Address: Institute of Space and Astronautical Science, Japan Aerospace Exploration Agency, 3-1-1 Yoshinodai, Sagamihara, Kanagawa 229-8510, Japan

the flux-bias corrected flux. Using the likelihood ratio analysis and the associated reliability, 44 FIR sources have been identified with radio sources. Optical identification of the 44 FIR/radio association is then conducted by using the accurate radio positions. Redshifts have been obtained for 29 out of 44 identified sources. One hyper-luminous infrared galaxy (HyLIRG) with $L_{FIR} > 10^{13}\mathrm{L}_{\odot}$ and four ultraluminous infrared galaxies (ULIRGs) with $L_{FIR} = 10^{12-13}\mathrm{L}_{\odot}$ are identified in our sample while the remaining 24 FIR galaxies have $L_{FIR} < 10^{12}\mathrm{L}_{\odot}$. The space density of the FIR sources at $z = 0.3-0.6$ is $4.6\times10^{-5}\mathrm{Mpc}^{-3}$, which is 460 times larger than the local value, implying a rapid evolution of the ULIRG population. Most of *ISO* FIR sources have $L(1.4GHz)/L(90\mu\mathrm{m})$ similar to star-forming galaxies ARP 220 and M82, indicating that the star-formation is the dominant mechanism for their FIR and radio luminosity.

At least seven of our FIR sources show evidence for the presence of an active galactic nucleus (AGN) in optical emission lines, radio continuum excess, or X-ray activity. Three out of five (60%) of the ULIRG/HyLIRGs are AGN galaxies, suggesting that the AGN fraction among the ULIRG/HyLIRG population may not change significantly between $z \sim 0.5$ and the present epoch. Five of the seven AGN galaxies are within the ROSAT X-ray survey field, and two are within the XMM-Newton survey fields. X-ray emission has been detected in only one source, 1EX030, which is optically classified as a quasar. The non-detection in the XMM-Newton 2-10 keV band suggests a very thick absorption column density of $3\times10^{24}\mathrm{cm}^2$ or $A_V \sim 1200$ mag obscuring the central source of the two AGN galaxies. Several sources have an extreme FIR luminosity relative to the optical R-band, $L(90\mu\mathrm{m})/L(R) > 500$, which is rare even among the local ULIRG population. While source confusion or blending might offer an explanation in some cases, they may represent a new population of galaxies with an extreme activity of star formation in an undeveloped stellar system – i.e., formation of bulges or young ellipticals.

Subject headings: infrared:galaxies — galaxies:evolution — galaxies: starburst

1. Introduction

The detection of the far-infrared Cosmic Infrared Background (CIRB) radiation by FIRAS and DIRBE on COBE was the important step toward understanding the physical property of the cosmological far-infrared (FIR) radiation. The CIRB was interpreted as the integrated emission by dust in the distant galaxies (Puget et al. 1996; Fixsen et al. 1998; Hauser et al. 1998) which set a relevant constraint on the evolution of cosmic sources. The CIRB is 10 times brighter than the expected intensity based on the assumption that the infrared emissivity of galaxies does not change with cosmic time (Takeuchi et al. 2001; Franceschini et al. 2001) and has comparable contribution to the total intensity as expected from the optical counts from the Hubble deep field and the Subaru deep field(Totani et al. 2001; Totani & Takeuchi 2002). Therefore the CIRB's excess suggests that

galaxies in the past were much more *active* in the FIR and that a substantial fraction of the total energy emitted by high-redshift galaxies were absorbed by dust and re-emitted at long wavelengths.

The SCUBA bolometer camera(Holland et al. 1999) on the sub-millimeter telescope JCMT was able to resolve at least half of the CIRB at wavelength of 850 μm into a population of very luminous infrared galaxies at $z \gtrsim 1$ (Smail, Ivision & Blain 1997; Hughes et al. 1998; Barger et al. 1998; Blain et al. 1999). ISOCAM mid-infrared surveys (Rowan-Robinson et al. 1997; Flores et al. 1999; Mann et al. 2002) have also reported a higher infrared luminosity density (thus a higher star formation rate) at $0.5 \lesssim z \lesssim 1$ than estimated by previous optical studies.

IRAS was able to detect infrared galaxies only to moderate redshifts ($z \sim 0.1$) with the exception of a few hyperluminous and/or lensed objects such as FSC 10214+4724 (Rowan-Robinson et al. 1991). The improvement of the sensitivity and the extension to the longer wavelength (170 μm) in FIR with ISOPHOT instrument onboard the *Infrared Space Observatory* (*ISO*) provides us with a new tool to study FIR emission from galaxies at the higher-redshifts than *IRAS*, and the exploration of the "optically dark side" of the star formation history through a deep FIR survey was the obvious next step.

The spectral energy distribution(SED) of actively star-forming galaxies peaks at $\lambda \sim 100$ μm. The "negative" k-correction makes observations at wavelengths longer than this FIR peak advantageous for detecting high-redshift galaxies. Furthermore, such measurements give the total luminosity without any model-dependent bolometric correction. Therefore several deep surveys were undertaken with the ISOPHOT at 90 μm and/or 170 μm. We performed a deep FIR survey of two fields in the Lockman Hole region in both 90 μm and 170 μm bands as a part of the Japanese/UH cosmology project (Kawara et al. 1998). A 170 μm survey of two fields in the southern Marano area and two fields in the northern ELAIS fields with a combined area of 4 square degrees constitute the FIRBACK program (Puget et al. 1999). A 90 μm survey in ELAIS (Efstathiou et al. 2000) covered 11.6 square degrees.

In order to explore the nature of *ISO* FIR sources in the Lockman Hole fields, we have identified counterparts to the sources at optical and radio wavelengths. We obtained their photometric characteristics and measured their redshifts in order to understand the genuine nature of *ISO* FIR sources in the Lockman Hole fields. Section 2 describes the observations and the data, Section 3 presents the method and results of the source identification, and Section 4 describes the discussions of *ISO* FIR sources in the Lockman Hole fields. The summary is presented in Section 5. Appendix describes the comparison of our catalogs with those in Rodighiero et al. (2003) and Rodighiero & Franceschini (2004), which reduced same data with their own method.

Throughout the paper, a flat Universe with $H_0 = 70$km s^{-1} Mpc^{-1}, $\Omega_M = 0.3$ and $\Omega_\lambda = 0.7$ is adopted.

2. Data

2.1. ISO far-infrared catalogs

Our FIR survey was performed in the ISOPHOT bands C_90 (90 μm for the reference wavelength) and C_160 (170 μm; see Kawara et al. 1998; Matsuhara et al. 2000; Kawara et al. 2004) in the Lockman Hole, where the HI column density is measured to be the lowest in the sky (Lockman et al. 1986) and thus the confusion noise due to the infrared cirrus is expected to be the lowest. The survey includes two fields named LHEX and LHNW, each of which covered approximately $44' \times 44'$square area. One of the fields, LHEX, was also the target of the ROSAT Lockman Hole ultra-deep HRI survey (Hasinger et al. 1998). The 90 μm and 170 μm observations with *ISO*(Kessler et al. 1996) and the data reduction are described in detail by Kawara et al. (1998, 2004). As shown in Figure 1, the ISOPHOT instrument (Lemke et al. 1996) was used to map a total area of $\sim$0.9 square degrees, consisting of two $44' \times 44'$ fields.

The *IRAF*[1] DAOPHOT package, which has been developed to perform stellar photometry in crowded fields(Stetson 1987), was used to perform the source extraction from the FIR maps. The survey images are very crowded, with two or more sources frequently appear blended. The FWHM measurements show that most bright sources subtends no more than two detector pixels, implying these sources are detected as point sources. The final 90 μm and 170 μm source catalogs with a signal to noise ratio of three or greater include 223 and 72 sources, respectively (Kawara et al. 2004). UGC 06009[2], which is the only IRAS source locating within our survey fields, was used for the flux scaling assuming F(90 μm)=1218 mJy and F(170 μm)=1133 mJy. The flux density of the cataloged sources ranges between 40 mJy and 400 mJy at 90 μm and between 90 mJy and 410 mJy at 170 μm.

The surface number densities of *ISO* FIR sources are sufficiently high (10-20 beams per source) that the derived quantities such as flux, position, completeness, and detection limits are significantly affected by source confusion. To evaluate these effects, Kawara et al. (2004) performed a set of simulations by adding artificial sources to the observed FIR maps. These simulations have shown that the measured fluxes of faint sources are indeed significantly overestimated and thus the correction for the flux bias is important. The following expressions are used for the correction:

$$F(90\mu\mathrm{m}) = 66 + 0.78 \times F^C(90\mu\mathrm{m}) + 0.0001 \times F^C(90\mu\mathrm{m})^2 \quad (1)$$

$$F(170\mu\mathrm{m}) = 160 + 0.32 \times F^C(170\mu\mathrm{m}) + 0.0007 \times F^C(170\mu\mathrm{m})^2 \quad (2)$$

where F and F^C denote the observed flux and the flux after correction for the bias effect, respectively. These expressions represent the results from the simulations by Kawara et al. (2004) with 2-3% accuracy for $F(90\mu\mathrm{m}) \geq 100$mJy or $F(170\mu\mathrm{m}) \geq 250$mJy, and 10% for $F(170\mu\mathrm{m}) < 250$mJy.

[1]IRAF is distributed by NOAO, which is operated by AURA, Inc., under contract to the NSF.

[2]If more accurate fluxes are measured in UGC 06009, the fluxes of FIR sources should be re-scaled accordingly.

Thus, the errors resulting from the expressions are small enough to be ignored. In this paper, we refer these corrected flux with Equ. (1) and (2).

Positional uncertainties are also estimated from these simulations. Position error depends on the brightness of FIR sources, and the dispersion in the measured position relative to the input position of the artificial sources, σ_{pos}, is larger toward fainter sources. The derived positional uncertainties from the simulations are $\sigma_{pos}(90\mu\mathrm{m}) \sim 20''$ for $F(90\mu\mathrm{m}) \sim 100\mathrm{mJy}$ and $\sigma_{pos}(170\mu\mathrm{m}) \sim 35''$ for $F(170\mu\mathrm{m}) \sim 200\mathrm{mJy}$. Their simulation also show that the completeness rapidly decrease as the flux decrease below 200 mJy; for example, the detection rate is 73% for sources with $F^C(90\mu\mathrm{m}) = 43\mathrm{mJy}$, and 64% for $F^C(170\mu\mathrm{m}) = 102\mathrm{mJy}$.

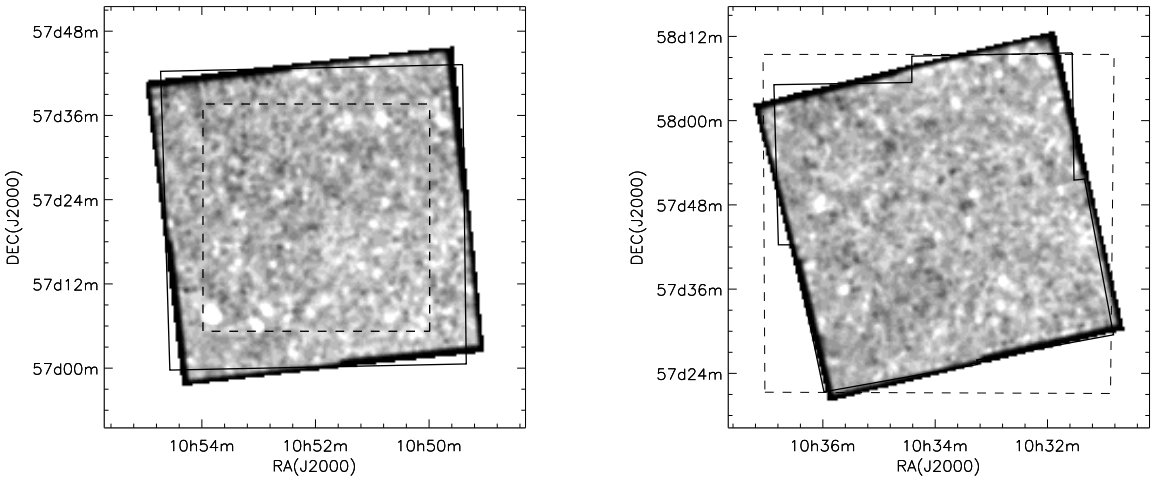

Fig. 1.— Survey areas superimposed on the *ISO* 90 μm images in the Lockman Hole. The LHEX field is shown on the left panel and LHNW on the right. The 170 μm fields are shown by solid lines, while dashed lines present the areas of our VLA 1.4 GHz sources which are used in this paper.

2.2. Radio observations

The *ISO* positional uncertainties of $20''$ - $35''$ are too large to search for optical counterparts directly because there are always several faint optical sources within each error circle. Thus we have taken a two-steps approach to identify FIR sources. In the first step, deep Very Large Array (VLA) 1.4 GHz imaging was performed and radio counterparts were found utilizing the well-known FIR-radio correlation (Condon 1992; Yun, Reddy, & Condon 2001). This approach may introduce a slight bias in favor of star-forming galaxies, but the AGN dominated sources are rare in general among the FIR selected sample (less than a few per cent, see Yun, Reddy, & Condon 2001). Once radio counterparts are known, then the positional uncertainty is reduced greatly to $\leq 1''$, and the second step of searching for optical counterparts becomes straight forward.

Deep 1.4 GHz continuum images of the LHNW and LHEX fields were obtained using the NRAO[3] VLA in the B-configuration in February 2000 and March-April 2001, respectively. Four separate pointings cover a $45' \times 45'$ square region centered on the two *ISO* survey fields. The angular resolution of the final images was about $5''$ (FWHM).

The rms noise achieved in the central $32' \times 32'$ mapping region of the LHEX field is $1\sigma \sim 15\mu$Jy. After combining additional data from the archive, the rms noise in the northeast quadrant centered near the ROSAT Deep Survey field (Hasinger et al. 1998) has been improved to $1\sigma \sim 10\mu$Jy. Our new VLA 1.4 GHz continuum image has about 2-3 times higher angular resolution and improved sensitivity over the previous observations by de Ruiter et al. (1997, $\theta \sim 12''$ and $1\sigma \sim 30\mu$Jy).

In the LHNW field, four separate pointings were also used. However, the imaging dynamic range in the LHNW field was severely limited by the presence of a bright radio source 3C 244.1 (4.2 Jy at 1.4 GHz) just outside the primary beam. Incomplete subtraction of the time varying PSF response resulted in a strong gradient of additional "noise" across the radio continuum image with a median value of $1\sigma \sim 30\mu$Jy in the image center. Therefore the radio source identification is dependent entirely on the local noise level, and the radio source catalog is complete only at the highest flux density level (~ 200 μJy). A more detailed descriptions of these VLA observations will be presented in a later paper (Yun et al., in preparation).

In this paper, we use 387 radio sources brighter than 60 μJy($\geq 4\sigma$) in the central $32' \times 32'$ region of the LHEX field and 76 sources in the entire LHNW field.

2.3. Optical R and $I-$band imaging

The $I-$band images of the two Lockman Hole fields were obtained using the 8K CCD Camera (Luppino et al. 1996) attached to the f/10 Cassegrain focus of the University of Hawaii $88''$ telescope

[3]The National Radio Astronomy Observatory is a facility of the National Science Foundation operated under cooperative agreement by Associated Universities, Inc.

on May 19-24 in 1999. This camera has a $18' \times 18'$ field of view. A 2×2-pixel binning was used yielding a sampling resolution of $0\farcs26$ pixel^{-1}. Nine pointings were used in each field to cover each field completely. The total exposure times were 14 and 21 minutes for the LHEX and LHNW fields, respectively. The seeing was about $\sim 0\farcs6$, and the 5σ detection limit reaches $I \sim 22-23$ depending on the location on the camera. Flux calibration was performed using the observations of SA103 and SA104 (Landolt 1992) with a systematic uncertainty of ~ 0.05 mag.

The deep $R-$band imaging of the both fields was carried out using the prime-focus camera, Suprime-Cam (Miyazaki et al. 2002) on the Subaru Telescope on March 19 in 2001. This camera has ten 4K×2K CCDs which provides a $34' \times 27'$ field of view with $0\farcs2$/pixel sampling. During our observing run, one CCD on the corner of the focal plane was not available. To cover entire *ISO* survey fields, four different pointings were used in each field. The exposure times were 30 minutes for the two pointings on the west and 25 minutes for the two pointing on the east. The wide-field optical corrector unit of the Suprime-Cam introduces the significant image distortion on the focal plane (e.g., $18''$ distortion at $20'$away from the center). This distortion is corrected using *IRAF* task GEOTRAN. The 5σ detection limit reaches 26.5 mag under typical seeing of $\sim 0\farcs8$. Flux calibration was performed using the observations of SA101 (Landolt 1992) and SA57 (Majewski et al. 1994) fields, with an estimated systematic uncertainty of ~ 0.08 mag.

The astrometry calibration of all optical images was obtained by comparing with the positions of stars in the United States Naval Observatory (USNO) A2.0 catalog (Monet et al. 1998). The astrometric uncertainty is estimated to be less than $1\farcs0$ for both R and $I-$band imaging.

2.4. Optical Spectroscopy

We performed spectroscopy of optical objects identified as radio counterparts to the FIR sources. Keck II telescope at the Mauna Kea Observatory and WIYN[4] 3.5m telescope at the Kitt Peak National Observatory were used with wide wavelength coverage, allowing many emission features for line identification.

2.4.1. Keck Observations

Spectroscopic observations with Keck II telescope were performed preferentially in order of optical brightness on March 30-31 in 2000 and on January 23-24 in 2001, using the Echelle Spectrograph and Imager (ESI:Sheinis et al. 2000) in the low-dispersion mode. The long slit was set to the optical center of the radio sources. The position angle of the slit was adjusted so that radio sources can be observed simultaneously from 3,900Å to 11,000Å. The slit width and length were

[4]The WIYN Observatory is a joint facility of the University of Wisconsin-Madison, Indiana University, Yale University, and the National Optical Astronomy Observatories.

$1''$(6.5 pixels) and $8'$, respectively. The spectral resolution ranged from 800 at the blue part to 300 per pixel at the red part. Exposure times used were between 300 sec and 5400 sec, depending on the optical brightness of the target sources. Standard data reductions were carried out using *IRAF*. Presence of emission or absorption lines was searched by eye. In this paper, we present 15 Keck II spectra of *ISO* FIR galaxies.

2.4.2. WIYN/HYDRA Observations

Spectroscopic observations were performed with the HYDRA multi-object spectrometer on the WIYN 3.5m telescope on February 19 in 2002 and February 6-7 in 2003, using the red cables ($2''$ diameter), the 316 line mm^{-1} grating with G5 filter, and the bench camera. The spectra cover the wavelength region 5,020−10,000 Å with a spectral resolution of 2.64 Å /pixel.

To cope with faint spectra in fiber-based spectroscopy, beam switching was used to efficiently remove sky emission features such as fringes and time-dependent airglow emission lines which are heavily blended in some cases. The beam switching requires two different pointings of the telescope. At pointing A, one half of 96 fibers available for HYDRA were centered on the targets while the others were set to the sky. At pointing B, the roles of fibers were switched. Beam switching was repeated 7 times every 30-minute, for a total on-source integration time of 210 minutes.

A specialized IRAF package DOHYDRA (Valdes 1995) was used to perform scattered light removal, spectra extraction, flat fielding, fiber throughput correction, and wavelengths calibration. Sky subtraction and subsequent spectrum co-adding require a careful treatment and are not fully supported by DOHYDRA. We thus developed special IDL routines to handle these tasks. Sky brightness, which is dominated by airglow emission lines, varies with airmass and time. The sky spectra were removed from the "on-target" fibers by using the sky background determined from the preceding and following "sky" fibers. Some scaling of the sky background were required to subtract time-dependent OH airglow emission. After subtracting the sky, the CCD fringes on "on-target" fibers reduced greatly. The resultant sky-subtracted spectra were then coadded to improve the signal-to-noise ratio. Extra-galactic emission lines were searched for by eye and by comparing the source spectra with the airglow spectra and distinguishing the residual airglow from real emission lines.

Spectra were obtained for a total of 50 objects in the two fields. The brightness of the target objects range between $R = 17$ and $R = 21$. Nine of the 50 objects are *ISO* FIR sources identified as radio counterparts. The remainder are other faint radio sources identified by the deep radio survey.

3. Radio Counterpart Identification

In this section, we illustrate the processes of identifying FIR sources with 1.4 GHz radio sources. Our 1.4 GHz survey has been carried out within the two *ISO* fields in the Lockman Hole. The areas where the present identification work was performed, are 1089 arcmin^2 in LHEX and 1552 arcmin^2 in LHNW. A typical position uncertainty of the radio source is $\sim 1''$, negligibly smaller than the typical *ISO* FIR position uncertainty.

The original catalogs by Kawara et al. (2004) contain sources with signal-to-noise ratios of 3σ or better. In the present work, we exclude faint sources which have $F^C(90\mu\mathrm{m}) < 43$mJy or $F^C(170\mu\mathrm{m}) < 102$mJy, which correspond to the catalog fluxes, $F(90\mu\mathrm{m}) < 100$mJy or $(170\mu\mathrm{m}) < 200$mJy. Accordingly, we adopt the position uncertainty of $1\sigma_{POS}(90\mu\mathrm{m}) = 18''$ and $1\sigma_{POS}(170\mu\mathrm{m}) = 30''$ (see Figure 4 of Kawara et al. 2004). Excluding UGC 06009, which is the only *IRAS* source within the survey areas and is used for the flux-calibration, the total numbers of 90 μm and 170 μm sources included in this study are 116 and 20, respectively.

Large FIR error circles and a high number density of faint radio sources ensures that there is a high probability of having confusing multiple radio sources within each FIR error circle. For example, 25 out of 49 ($\sim 50\%$) of the 90 μm sources in the LHEX field have two or more radio sources with in a 3σ error circle ($54''$ radius; see Table 1). Thus the task at hand is to reject confusing radio sources which are within the error circle by chance, by quantifying the reliability of every identification through a statistical approach as discussed below.

3.1. Likelihood ratio analysis

The likelihood ratio analysis using cross-association (de Ruiter, Arp, & Willis 1977; Sutherland & Saunders 1992; Mann et al. 1997; Rutledge et al. 2000) is a commonly used technique for identifying sources in crowded fields. Here, we adopt the prescription given by Rutledge et al. (2000). It is assumed that each FIR source is physically associated with either one radio source or none. It is also assumed that there are two types of FIR sources – one type has one real radio counterpart while the second type has no real radio counterpart. Because of the source confusion due to the high number density of radio sources, in many cases there are one or more radio sources found within a 3σ error circle centered at the FIR position.

To assess the reliability of individual identifications, we begin with the likelihood ratio which is described by de Ruiter, Arp, & Willis (1977) and Wolstencroft et al. (1986). Position uncertainty and number density of radio sources are known, and it is assumed that each source has one or more candidate radio counterparts within a 3σ error circle. A dimensionless angular distance r, between the FIR and radio positions, is defined as,

$$r^2 = \left(\frac{\Delta\theta^2}{\sigma_{pos}^2 + \sigma_R^2} \right) \tag{3}$$

where $\Delta\theta$ is the positional differences between the FIR and radio sources, and σ_R is the standard deviation of the radio positions. As already discussed, σ_R is typically $\sim 1''$ and negligible when compared with FIR error $\sigma_{pos} \sim 18''$ or $30''$. Thus we adopt $r = \Delta\theta/\sigma_{pos}$. The surface density of radio sources, $n(f)$, is the number density of radio sources with 1.4 GHz flux equal to or greater than f, and it is adopted from Richards (2000).

Assuming that a FIR source and its *true* radio counterpart are located at the same position, the measured separation r is due to the FIR position uncertainty. Then, the probability, dp_{id}, of having a real radio counterpart at a distance between r and $r + dr$ from the FIR sources, is $dp_{id} = r\exp(-r^2/2)dr$. The probability, dp_c, of finding a first confusing object between r and $r + dr$ from the FIR source is a product of two probabilities; the probability of not having a counterpart within r, which is given by $e^{-\pi r^2\sigma^2 n(f)}$, and the probability of a confusing object between r and $r + dr$, which is $1 - e^{-2\pi r dr\sigma^2 n(f)} \sim 2\pi r\sigma^2 n(f)dr$. Thus the probability, dp_c, is expressed as $dp_c = 2\pi\sigma^2 n(f)rdr \times \exp\left(-\pi r^2\sigma^2 n(f)\right)$.

The likelihood ratio is defined as the ratio of dp_{id}/dp_c, and

$$LR(r, f) = \frac{1}{2\pi\sigma^2 n(f)} \exp\left(-\frac{r^2}{2} + \pi r^2\sigma^2 n(f)\right). \tag{4}$$

For each FIR source, LR is calculated for all radio sources within the 3σ error circle. Then the frequency distribution $N(LR)$ is computed. Figures 2 and 3 show the distribution of LR as thick-lined histograms for 90 μm and 170 μm. The LR distribution was derived only in the LHEX field because the LHNW field radio data suffers from a non-uniform noise and complex source statistics.

Once the distribution of the likelihood ratio LR is determined, a reliability R for identification with LR can be quantified as

$$R(LR) = \frac{N_{true}(LR)}{N_{true}(LR) + N_{false}(LR)}, \tag{5}$$

where $N_{true}(LR)$ and $N_{false}(LR)$ are the numbers of $true$ and $false$ radio counterparts, respectively. In practice, however, it is generally unknown which radio source is the real counterpart or what N_{true} and N_{false} are.

The denominator in Equ. (5) can be re-written as

$$N_{true}(LR) + N_{false}(LR) = N_{source}(LR), \tag{6}$$

where $N_{source}(LR)$ is the total number of radio sources with LR in the field. In general N_{true} is not known, but we can estimate N_{true} from the difference between N_{source} and N_{ran}, where N_{source} and N_{ran} are the numbers of radio sources in regions containing FIR sources and containing no FIR sources, respectively. There is not enough area free from ISO FIR sources because of the high source density and large positional uncertainty of the ISO FIR sources. We estimated $N_{ran}(LR)$ by randomly assigning positions to radio sources in the catalog. These simulations are repeated

100 times and averaged. The resultant $N_{ran}(LR)$ is shown as shaded histograms in Figures 2 and 3. Comparing the observed distributions $N_{source}(LR)$ with the randomly generated $N_{ran}(LR)$, it is clear that $N_{source}(LR)$ has excess over $N_{ran}(LR)$ for $\log(LR) \gtrsim 0$.

Our radio catalog consists of both kinds of radio sources: "real" and "false" counterparts of FIR sources. Thus, $N_{ran}(LR)$ should be greater than $N_{false}(LR)$. Using $N_{ran}(LR)$, $N_{true}(LR)$ is represented as;

$$N_{true}(LR) \geq N_{source}(LR) - N_{ran}(LR). \tag{7}$$

Here we introduce the modified reliability $\tilde{R}(LR)$, as defined by

$$\tilde{R}(LR) = \frac{N_{source}(LR) - N_{ran}(LR)}{N_{source}(LR)} \leq \frac{N_{true}(LR)}{N_{source}(LR)} = R(LR). \tag{8}$$

$\tilde{R}$ is plotted on Figures 4 and 5 together with quadratic approximations of $\tilde{R}$ as a function of $\log(LR)$.

As seen in Eqa. (8), $\tilde{R}(LR)$ is less than the true reliability $R(LR)$. The typical ratio $R/\tilde{R}$ for $log(LR) > 0$ can be estimated as follows. According to Table 1, the number of radio sources is 387, and 27 of them are identified with 90 μm sources. Thus, the fraction of true radio counterpart is 27/387. Because of randomly assigned radio positions in the simulation, this fraction should be independent of LR. In Figure 2, $N_{source}(log(LR) > 0) = 69$ and $N_{ran}(log(LR) > 0) = 28$. Then, $N_{false}(log(LR) > 0)$ is $28 \times (1. - 27/387)$. Substituting these into Eqa. (5) and (8), $R = [69 - 28 \times (1. - 27/387)]/69 = 0.62$ and $\tilde{R} = [69 - 28]/69 = 0.59$. Thus, $R(LR)/\tilde{R}(LR) = 1.05$ for $log(LR) > 0$, and the difference between the true and modified reliability R and $\tilde{R}$ is small.

Where more than one radio sources are found within a 3σ error radius, the sum of R of individual sources frequently exceeds unity. Thus, it is necessary to normalize R so that the sum of R plus the probability of having no radio counterpart is unity. Suppose that there are M radio candidates, one of which or none of which is a true radio counterpart. $P_{id,i}$ and P_{no-id} denote the probability that the $i-th$ candidate is the uniquely true radio counterpart and none of radio candidates is the real radio counterpart. Then the probability of the $i-th$ candidate to be "true" and "false" are $\tilde{R}_i$ and $(1 - \tilde{R}_i)$, respectively. Thus, P_{no-id} and $P_{id,i}$ are:

$$P_{no-id} = \frac{\Pi_{j=1}^{M}(1 - \tilde{R}_j)}{S}, \tag{9}$$

and

$$P_{id,i} = \frac{\left[\tilde{R}_i \Pi_{j\neq i}^{M}(1 - \tilde{R}_j)\right]}{S}, \tag{10}$$

where S is a normalization factor, specific to each ISO FIR source. Setting the sum of all the probabilities to unity gives

$$P_{no-id} + \sum_{i=1}^{M} P_{id,i} = 1. \tag{11}$$

The normalization factor S is derived as,

$$S = \sum_{i=1}^{M} \tilde{R}_i \Pi_{j\neq i}^{M}(1-\tilde{R}_j) + \Pi_{j=1}^{M}(1-\tilde{R}_j). \quad (12)$$

3.2. Identification

The main criterion adopted for a true radio counterpart identification is the condition $P_{id} > P_{no-id}$. The results are summarized in Table 1. In the LHEX field, 27 of 49 90 μm sources are identified with radio sources. The identification rate is higher in bright sources than in fainter sources as shown in Fig 6. The rate is 81% (13/16) for 90 μm sources brighter than 100mJy while it is reduced to 42% (14/33) for sources fainter than 100mJy. This is due to poorer positional accuracy (Kawara et al. 2004) for fainter sources. Seven of nine 170 μm sources in the LHEX field meet our criterion. Five of them have the same identification as their 90 μm counterpart. One exception is 1EX085/2EX068, for which the 90 μm identification is given priority for the reason described at the end of this section. While one additional source, 2EX016, does not meet our identification criterion, the identified radio source for the associated 90 μm source, 1EX034, is regarded as the true counterpart. In summary, a total of eight 170 μm sources are identified.

Because of the higher effective noise in the radio continuum image of the LHNW field, there are only a few cases where two or more radio candidates are found. To proceed with the same source identification criterion, the reliability functions derived from the LHEX field were applied to the LHNW field as well. As a result, 15 of 67 sources and 5 of 11 sources in 90 μm and 170 μm are identified with radio sources. The identification rate is 48% (11/23) for 90 μm sources brighter than 100mJy and 9% (4/44) for fainter than 100mJy.

Optical identification was made by searching optical objects within a $2''$ radius of the radio counterpart on the Subaru R-band image. If no objects are found, bright objects ($R < 20$) are searched within a $5''$ radius from the radio counterpart. All of the radio counterparts are identified with an optical object. The dispersion of separation between radio and optical sources is only $0''.6$. All of the optical counterparts are galaxies except for 1EX030, which is a point-like source showing broad emission lines characteristic of a quasar. The R-band images are shown together with 1.4 GHz contours in Figure 7.

Individual radio counterparts are listed together with the optical data in Table 2 and 3 for the 90 μm and 170 μm sources. In columns 1 & 2, names of the 90 and 170 μm sources are given. In column 3, a name of radio sources are given in order of appearance. In columns 4 & 5, the radio coordinates are given in the J2000 system. In columns 6 & 7, the FIR fluxes are given including the correction for the bias effect(Equ. (1) and (2)). In column 8, the 1.4 GHz flux is given in μJy. In columns 9 & 10, R and $I-$band magnitudes are given in Vega system. Column 11 lists the angular distance of the radio counterpart from the position of the FIR source in arcsec. In columns 12-14, LR, P_{id}, and P_{no-id} are given. If more than one radio sources meet the identification criterion

$P_{id} > P_{no-id}$, then all of radio sources are listed in the tables. Table 4 summarizes the optical and radio properties of the identified *ISO* FIR sources.

Source identification is complicated in several cases, and additional details are discussed below.

1EX076. 1EX076 has three radio candidates: two bright galaxies (REX11,REX13) and one bright radio source (REX12). REX11, REX12 and REX13 are shown at the $R-$band image in Figure 8(a) REX11 and REX13 are a interacting galaxies pair at the same redshift of $z = 0.073$. Moreover, REX11 is the closest to 1EX076 and its reliability is the highest among the three objects. REX11 is thus the most likely optical counterpart of this FIR source although there might also be a significant contribution from REX13.

1EX034/2EX016. Although 2EX016 does not have any radio candidate that meets our identification criterion, 1EX034 is identified with a radio source. This radio source is thus regarded as the counterpart of 1EX034/2EX036.

1EX269/2EX047. As shown in Figure 8(b), 1EX269 and 2EX047 have three common candidates (REX21, 22, & 23). REX21 is regarded as the counterpart because REX21 has the highest reliability among the three.

1EX085/2EX068. 2EX068 has two radio candidates (REX07, REX32) meeting the criterion, while 1EX085 has only one candidate (REX07) meeting the identification criterion(Figure 8(c)). Thus, 2EX068 is identified with REX07.

1NW025/2NW006. 1NW025($F^c(90\mu\mathrm{m})$ = 91mJy; RA=10:35:16.2, Dec.=+57:33:19 at J2000) does not have any candidates meeting the criterion while 2NW006($F^c(170\mu\mathrm{m})$ = 158mJy; RA=10:35:17.0, Dec.=+57:33:22 at J2000) is identified with a relatively bright radio source (F(1.4 GHz)=2587 μJy; RA=10:35:23.30, Dec.=+57:32:49.6 at J2000). The separation between 1NW025 and 2NW006 is only $8''$. Since the identified source is too far (3.6 σ_{pos}) from the 1NW025 position. We regard 1NW025/2NW006 as unidentified.

Table 1. Radio sources within a 3σ FIR error circle: a $54''$ radius at 90 μm and $90''$ at 170 μm

	Area			Association			Identification[f]	
	(arcmin^2)	N_{all}[a]	N_R[b]	N_S[c]	N_M [d]	$\frac{N_S+N_M}{N_{all}}$[e]	N_{id}	N_{id}/N_{all}
LHEX 90 μm	1089	49	387	15	25	0.82	27	0.55
LHEX 170 μm	1089	9	387	0	9	1.00	8	0.89
LHNW 90 μm	1552	67	76	17	2	0.28	15	0.22
LHNW 170 μm	1552	11	76	5	2	0.63	5	0.45

[a]The number of FIR sources for this study

[b]The number of radio sources for this study.

[c]The number of FIR sources with a single radio source within its FIR error circle.

[d]The number of FIR sources with multiple radio sources within its FIR error circle.

[e]Fraction of FIR sources with one or more radio counterpart candidates.

[f]Results of the source identification. See section § 3.2.

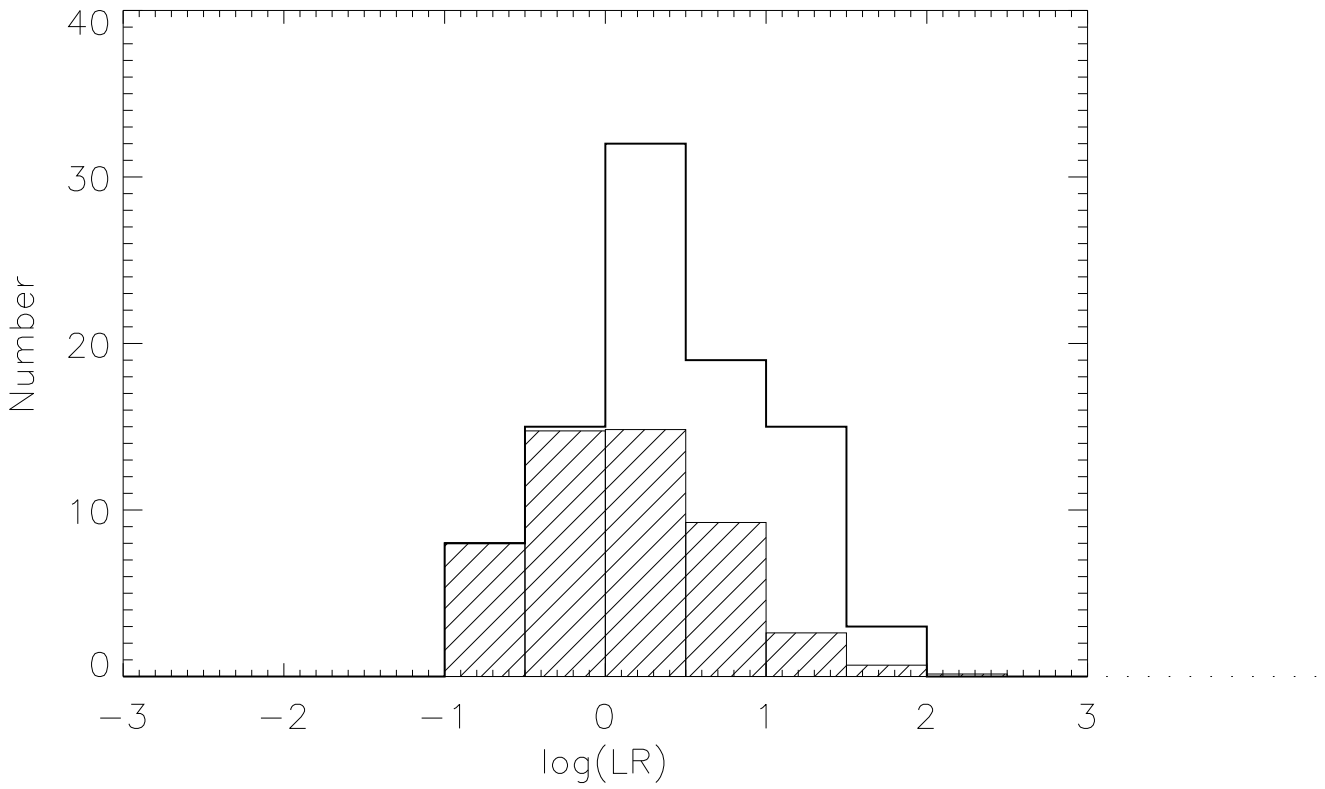

Fig. 2.— Number distributions as a function of LR for radio sources lying within the 3σ error circle centered at the ISO 90 μm source position. The empty histogram shows the observed distribution $N_{source}(LR)$ while the shaded histogram shows the background distribution obtained from assigning randomly generated positions to the radio sources $N_{ran}(LR)$.

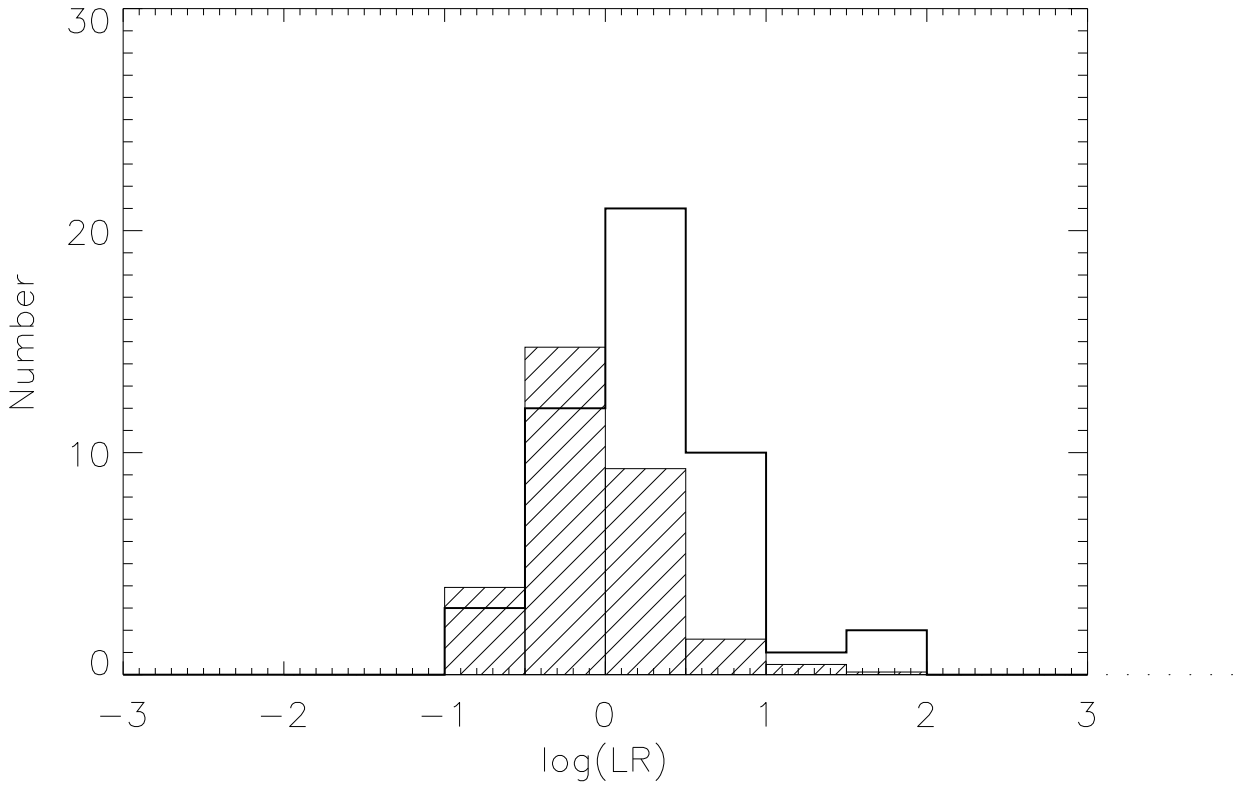

Fig. 3.— Same as Fig. 2 but for the 170 μm sources.

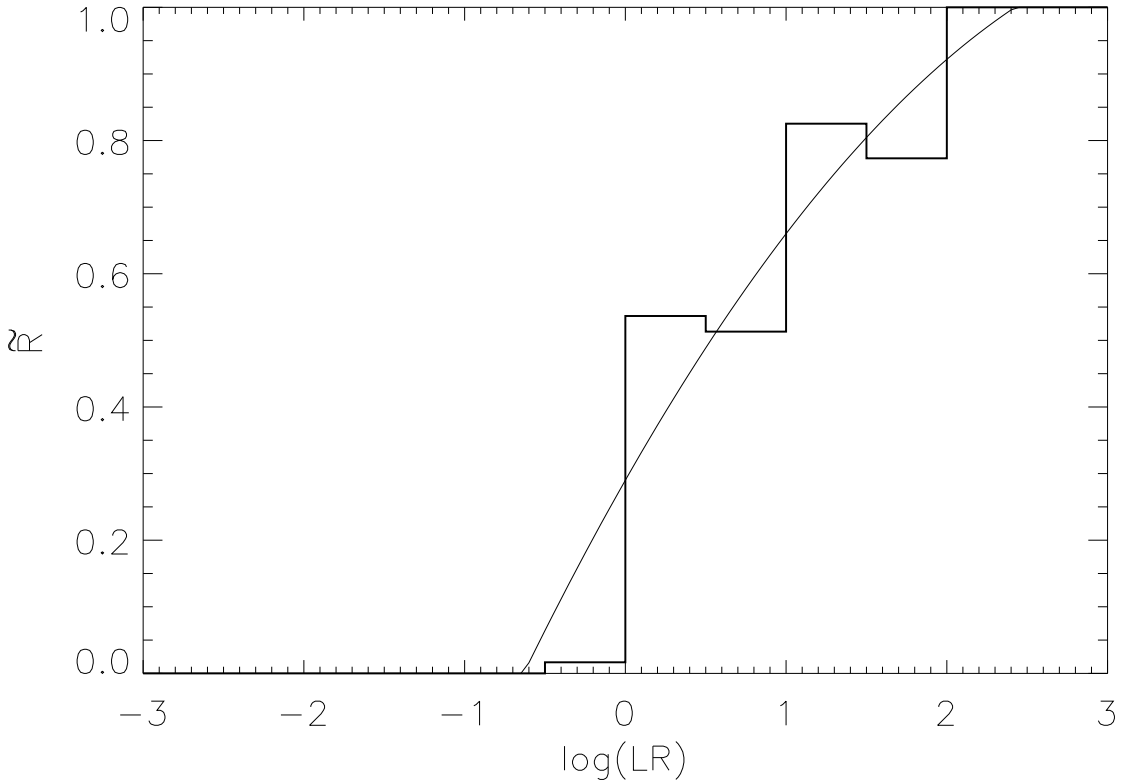

Fig. 4.— Modified reliability $\tilde{R}$ as a function of LR for the 90 μm sources. The thin line is a fit to $\tilde{R}$: $\tilde{R} = 0.29 + 0.42x - 0.05x^2$ where $x = \log(LR)$. This function is used as an input for deriving the probability for source identification $P_{id,i}$ and unidentification P_{no-id}.

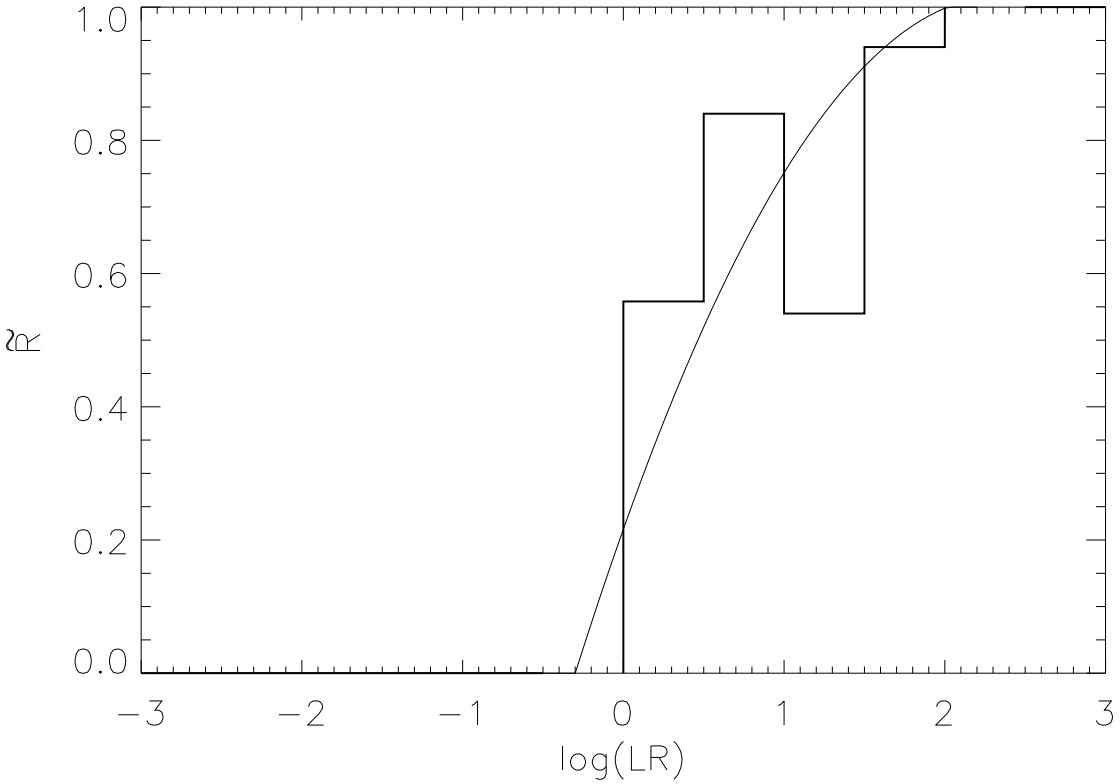

Fig. 5.— Same as Fig. 4 but for the 170 μm sources. The thin curve is $\tilde{R} = 0.21 + 0.68x - 0.14x^2$ where $x = \log(LR)$.

Table 2. A list of the identified far-infrared source at 90μm.

(C_90)	Name (C_160)[a]	(1.4 GHz)	RA[b] (J2000)	Dec.[b] (J2000)	$F^C(90\mu m)$[c] (mJy)	$F^C(170\mu m)$[c] (mJy)	$F_{1.4GHz}$ (μJy)	R	I	*dist.* (arcsec)	LR	P_{id}	P_{no-id}
					LHEX								
1EX153	...	REX01	10 50 02.13	+57 16 21.3	56 ± 16	...	143	21.8	21.5	13	6.88	0.48	0.31
1EX116	...	REX02	10 50 12.54	+57 11 36.8	107 ± 12	...	377	24.1	>22.0	34	4.41	0.41	0.35
1EX117	...	REX03	10 50 19.73	+57 28 13.2	66 ± 12	...	227	19.1	18.5	16	9.99	0.43	0.22
1EX088	...	REX04	10 50 37.55	+57 28 44.9	104 ± 23	...	392	19.8	19.0	9	21.48	0.67	0.21
1EX048	2EX004	REX05	10 50 41.99	+57 07 06.4	254 ± 19	407± 30	346	16.3	15.8	12	17.15	0.67	0.25
1EX041	2EX013	REX06	10 50 52.39	+57 35 07.5	310 ± 80	343± 88	182	<15.3[d]	14.7	9	10.01	0.42	0.22
1EX085	2EX068	REX07	10 50 56.57	+57 16 31.2	73 ± 24	125± 14	242	20.5	19.8	14	11.53	0.54	0.26
1EX084	...	REX08	10 51 00.90	+57 20 36.0	114 ± 21	...	261	24.3	22.0	17	10.69	0.57	0.28
1EX081	2EX115	REX09	10 51 13.44	+57 14 26.2	88 ± 16	212± 47	611	20.0	19.1	5	34.36	0.72	0.16
1EX038	...	REX10	10 51 19.66	+57 28 04.0	43 ± 13	...	94	24.5	>22.0	18	3.65	0.51	0.49
1EX076	...	REX11	10 51 28.07	+57 35 02.4	152 ± 17	...	303	16.6	16.3	18	11.53	0.34	0.16
		REX12	10 51 20.86	+57 35 32.6			7177	24.9	>22.0	47	7.99	0.27	0.16
		REX13	10 51 25.68	+57 35 44.2			497	15.5	15.2	32	6.59	0.24	0.16
1EX075	...	REX14	10 51 34.41	+57 33 59.9	53 ± 18	...	110	16.6	16.0	21	3.72	0.41	0.39
1EX100	...	REX15	10 51 37.01	+57 29 40.8	54 ± 14	...	1901	22.3	21.7	34	15.00	0.57	0.23
1EX047	2EX036	REX16	10 51 52.38	+57 09 50.1	113 ± 21	252± 46	2642	22.2	21.2	23	50.76	0.76	0.13
1EX034	2EX016	REX17	10 52 07.19	+57 07 44.8	124 ± 18	184± 27	159	17.1	16.5	7	9.13	0.60	0.33
1EX130	...	REX18	10 52 31.82	+57 09 27.1	54 ± 12	...	123	22.9	21.7	17	5.07	0.31	0.24
1EX030	...	REX19	10 52 39.55	+57 24 31.0	132 ± 29	...	136	17.7	17.6	5	8.01	0.46	0.27
1EX028	...	REX20	10 52 52.76	+57 07 53.7	150 ± 33	...	260	17.5	16.8	32	3.80	0.52	0.48
1EX269	2EX047	REX21	10 52 56.82	+57 08 25.7	206 ± 53	163± 42	439	16.8	16.2	22	13.29	0.39	0.17
		REX22	10 52 52.76	+57 07 53.7			260	17.5	16.8	30	4.55	0.20	0.17
		REX23	10 52 58.00	+57 08 34.8			337	22.7	21.0	34	3.94	0.18	0.17
1EX062	...	REX24	10 53 01.36	+57 05 42.9	399 ± 29	...	705	16.9	16.3	4	39.33	0.83	0.17
1EX179	...	REX25	10 53 18.96	+57 21 40.4	129 ± 29	...	247	17.1	16.6	7	14.48	0.60	0.25
1EX126	...	REX26	10 53 22.83	+57 15 00.0	74 ± 16	...	261	21.4	20.2	5	15.77	0.57	0.22
1EX026	...	REX27	10 53 25.30	+57 29 11.4	90 ± 20	...	507	17.6	17.4	8	27.18	0.76	0.21
1EX025	...	REX28	10 53 28.01	+57 11 15.5	67 ± 15	...	300	18.2	17.6	10	15.91	0.72	0.28
1EX125	...	REX29	10 53 26.68	+57 14 05.9	83 ± 12	...	226	19.3	18.7	15	10.25	0.66	0.34
1EX112	...	REX30	10 53 42.08[e]	+57 30 26.1[e]	74± 25	...	335	24.6	>22.0	18	13.05	0.70	0.30
1EX055	...	REX31	10 53 57.76	+57 23 47.1	61± 20	...	119	22.5	21.3	18	4.59	0.37	0.31
					LHNW								
1NW130	2NW013	RNW01	10 31 23.03	+57 42 26.4	172 ± 19	359 ± 53	677	20.0	19.1	10	32.89	0.81	0.19

Table 2—Continued

(C_90)	Name (C_160)[a]	(1.4 GHz)	RA[b] (J2000)	Dec.[b] (J2000)	$F^C(90\mu m)$[c] (mJy)	$F^C(170\mu m)$[c] (mJy)	$F_{1.4GHz}$ (μJy)	R	I	*dist.* (arcsec)	LR	P_{id}	P_{no-id}
1NW034	...	RNW02	10 31 47.58	+57 49 27.5	119± 22	...	200	20.5	19.7	24	5.58	0.58	0.42
1NW077	...	RNW03	10 32 05.80	+58 02 39.2	122± 22	...	447	20.2	19.0	9	24.22	0.77	0.23
1NW192	2NW003	RNW04	10 32 49.52	+57 37 07.9	226± 33	262 ± 39	420	17.1	16.5	9	22.94	0.77	0.23
1NW031	...	RNW05	10 33 15.43	+57 31 01.8	128± 28	...	408	21.6	20.6	34	4.50	0.54	0.46
1NW021	2NW005	RNW06	10 33 20.20	+57 49 13.1	127± 23	192 ± 50	343	18.7	18.0	11	17.71	0.74	0.26
1NW062	...	RNW07	10 33 30.28	+57 42 25.0	57± 15	...	143	19.9	19.1	15	6.48	0.60	0.40
1NW100	...	RNW08	10 33 52.36	+57 27 01.4	62± 9	...	292	17.7	17.3	19	10.62	0.67	0.33
1NW030	...	RNW09	10 33 58.71	+57 43 17.3	105± 19	...	915	17.3	16.6	11	41.41	0.83	0.17
1NW272	2NW009	RNW10	10 33 59.09	+57 29 52.4	91± 20	199 ± 29	1493	20.8	19.1	15	53.34	0.86	0.14
1NW026	...	RNW11	10 35 13.69	+57 34 44.6	51± 13	...	434	21.9	21.0	9	23.56	0.77	0.23
1NW092	...	RNW12	10 36 04.05	+57 48 12.2	205± 38	...	267	19.5	18.9	20	9.41	0.65	0.35
1NW023	...	RNW13	10 36 06.52	+57 47 02.1	169± 31	...	670	16.7	16.2	23	17.69	0.72	0.26
1NW022	...	RNW14	10 36 11.61	+57 43 21.1	101± 22	...	262	16.3	15.6	3	16.19	0.72	0.28
1NW133	...	RNW15	10 36 15.41	+57 39 14.7	169± 37	...	338	16.8	16.1	13	16.31	0.72	0.28

[a]The positional association of FIR sources in both bands come from Kawara et al. (2004).

[b]The J2000 coordinates come from the VLA 1.4 GHz radio data.

[c]The bias corrected flux density using Equ. (1.)

[d]$R-$band photometry is not available due to saturation.

[e]The positional difference between optical and radio is $3\farcs0$, which is larger than the typical error $0\farcs6$.

Table 3. A list of the identified far-infrared source at 170 μm .

(C_160)	Name (C_90)[a]	(1.4 GHz)	RA[b] (J2000)	Dec.[b] (J2000)	$F^C(170\mu m)$[c] (mJy)	$F^C(90\mu m)$[c] (mJy)	$F_{1.4GHz}$ (μJy)	R	I	dist. (arcsec)	LR	P_{id}	P_{no-id}
					LHEX								
2EX004	1EX048	REX05	10 50 41.99	+57 07 06.4	407± 30	254 ± 19	346	16.3	15.8	16	6.79	0.51	0.25
2EX013	1EX041	REX06	10 50 52.39	+57 35 07.5	343± 88	310 ± 80	182	15.3	14.7	22	3.34	0.39	0.35
2EX068	1EX085	REX32	10 50 56.54	+57 15 32.7	125± 14	73 ± 24	462	22.8	22.3	27	7.03	0.45	0.21
		REX07	10 50 56.57	+57 16 31.2		...	242	20.5	19.8	34	3.19	0.22	0.21
2EX115	1EX081	REX09	10 51 13.44	+57 14 26.2	212± 47	88 ± 16	611	20.0	19.1	40	5.74	0.50	0.28
2EX036	1EX047	REX16	10 51 52.38	+57 09 50.1	252± 46	113 ± 21	2642	22.2	21.2	37	19.85	0.77	0.14
2EX016	1EX034	REX17	10 52 07.19	+57 07 44.8	184± 27	124± 18	159	17.1	16.5	32	2.36	0.30[f]	0.39[f]
2EX015	...	REX33	10 52 37.38[g]	+57 31 03.5[g]	151 ± 38	...	14667	20.7	19.1	33	82.74	0.96	0.01
2EX047	1EX269	REX21	10 52 56.82	+57 08 25.7	163 ± 42	206 ± 53	439	16.8	16.2	29	6.25	0.33	0.18
		REX22	10 52 52.76	+57 07 53.7		...	260	17.5	16.8	28	4.11	0.23	0.18
		REX23	10 52 58.00	+57 08 34.8		...	337	22.7	21.0	41	3.37	0.19	0.18
					LHNW								
2NW013	1NW130	RNW01	10 31 23.03	+57 42 26.4	359 ± 53	172 ± 19	677	20.0	19.1	19	11.50	0.76	0.24
2NW003	1NW192	RNW04	10 32 49.52	+57 37 07.9	262 ± 39	226 ± 33	420	17.1	16.5	27	6.43	0.66	0.34
2NW005	1NW021	RNW06	10 33 20.20	+57 49 13.1	192 ± 50	127 ± 23	343	18.7	18.0	13	6.99	0.62	0.30
2NW004	...	RNW16	10 33 41.32	+58 02 21.1	165 ± 41	...	380	18.0	17.2	26	6.00	0.65	0.35
2NW009	1NW272	RNW10	10 33 59.09	+57 29 52.4	199 ± 29	91 ± 20	1493	20.8	19.1	31	16.01	0.82	0.18

[Note] Same as Table 2.

[f] The radio source of 2EX016 does not meet our criterion, $P_{id} > P_{no-id}$. However the associated 90 μm source, 1EX034, is identified with a radio source, which is regarded as the counterpart of 1EX034/2EX016.

[g] The position comes from the optical image because the associated radio source position is dominated by the bright, extended radio lobes.

Table 4. A list of identified FIR sources

Name (C_90)	Name (C_160)	$F^C(90\mu m)$ (mJy)	$F^C(170\mu m)$ (mJy)	$\frac{L(1.4GHz)}{L(90\mu m)}$ (10^{-7})	$\frac{L(90\mu m)}{L(R)}$	z[a]	$\log(L_{FIR})$ ($L_\odot$)	Nature[b]
1EX153	...	56	...	11.5	69.2	...	...	...
1EX116	...	107	...	16.0	1063.3	...	...	...
1EX117	...	66	...	15.6	6.4	...	...	...
1EX088	...	104	...	17.0	20.3	0.363K	11.7	...
1EX048	2EX004	254	407	6.1	2.0	0.091K	10.9	...
1EX041	2EX013	310	343	2.6	<0.9	0.028K	9.8	...
1EX085	2EX068	73	125	15.0	26.3	0.396K	11.7	i
1EX084	...	114	...	10.3	1360.4	...	...	...
1EX081	2EX115	88	212	31.1	20.2	0.362K	11.8	...
1EX038	...	43	...	9.8	626.1	...	...	...
1EX076	...	152	...	9.0	1.5	0.073H	10.3	i,HII
1EX075	...	53	...	9.2	0.5	0.074H	10.1	...
1EX100	...	54	...	157.9	106.9	...	...	AGN
1EX047	2EX036	113	252	105.0	200.2	...	...	AGN
1EX034	2EX016	124	184	5.8	2.0	0.123K	10.8	...
1EX130	...	54	...	10.3	187.1	...	...	...
1EX030	...	132	...	4.6	3.8	1.110H	13.1	Quasar
1EX028	...	150	...	7.8	3.4	0.163K	11.0	...
1EX269	2EX047	206	163	9.6	2.6	0.080K	10.5	...
1EX062	...	399	...	7.9	5.3	0.080K	10.8	...
1EX179	...	129	...	8.6	2.2	0.133H	10.8	...
1EX126	...	74	...	15.9	61.3	...	...	...
1EX026	...	90	...	25.3	2.4	0.029H	9.3	HII
1EX025	...	67	...	20.3	3.0	0.162H	10.8	i,AGN
1EX125	...	83	...	12.2	10.6	0.231H	11.2	...
1EX112[c]	...	74	...	20.3	1156.1	...	...	...
1EX055	...	61	...	8.8	145.1	...	...	...
...	2EX015	...	151	> 1527.9	<19.2	0.710K	12.3	AGN
1NW130	2NW013	172	359	17.7	40.0	0.502K	12.4	...
1NW034	...	119	...	7.5	45.7	...	...	...
1NW077	...	122	...	16.5	32.8	...	...	i?
1NW192	2NW003	226	262	8.4	3.6	0.115K	11.0	...
1NW031	...	128	...	14.3	125.6	...	...	...
1NW021	2NW005	127	192	12.2	8.7	0.240K	11.5	i
1NW062	...	57	...	11.3	12.3	0.498B	11.9	...
1NW100	...	62	...	21.3	1.7	0.182B	10.9	...
1NW030	...	105	...	39.3	2.0	0.263K	11.4	...
1NW272	2NW009	91	199	73.5	43.7	0.469K	12.1	AGN
1NW026	...	51	...	38.1	68.8	...	...	i?
1NW092	...	205	...	5.9	29.5	0.511B	12.4	...
1NW023	...	169	...	17.8	1.9	0.044B	9.9	...
1NW022	...	101	...	11.7	0.8	0.093K	10.4	...
1NW133	...	169	...	9.0	2.1	0.114H	10.7	AGN
...	2NW004	...	165	>39.5	<1.6	0.075H	10.2	...

[a]Characters represent the used telescope; (K) Keck II/ESI data, (H) WIYN/HYDRA data and (B) from A. Barger (private communication)

[b](i) represents interacting galaxy system from Figure 7. (HII) shows the sources with HII-region-like spectra. (AGN) shows the sources with AGN/LINER-like spectra or radio excess. See section § 4.3 for details.

[c]An alternative ID is a $R = 19.6$ galaxy at $z = 0.586$ which is known to be an X-ray sources at RA=10:53:39.70 and Dec=+57:31:05.0(J2000)(Lehmann et al. 2001).

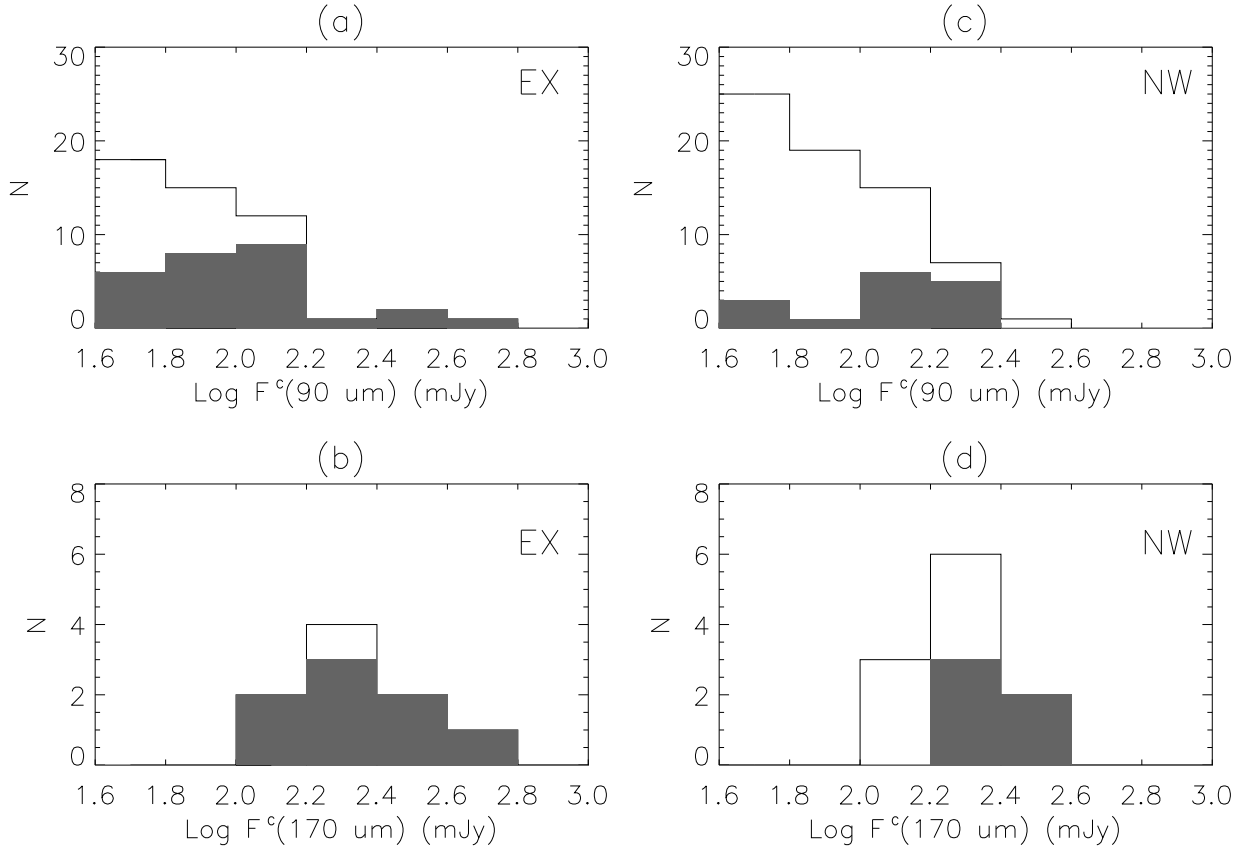

Fig. 6.— Histograms of FIR sources. The empty histograms show the distributions of all FIR sources used for the identification analysis, while the shaded histograms represent the distribution of identified FIR sources. Panel (a) is for 90 μm sources in the LHEX field, (b) for 170 μm sources in LHEX, (c) for 90 μm sources in LHNW, and (d) for 170 μm sources in LHNW.

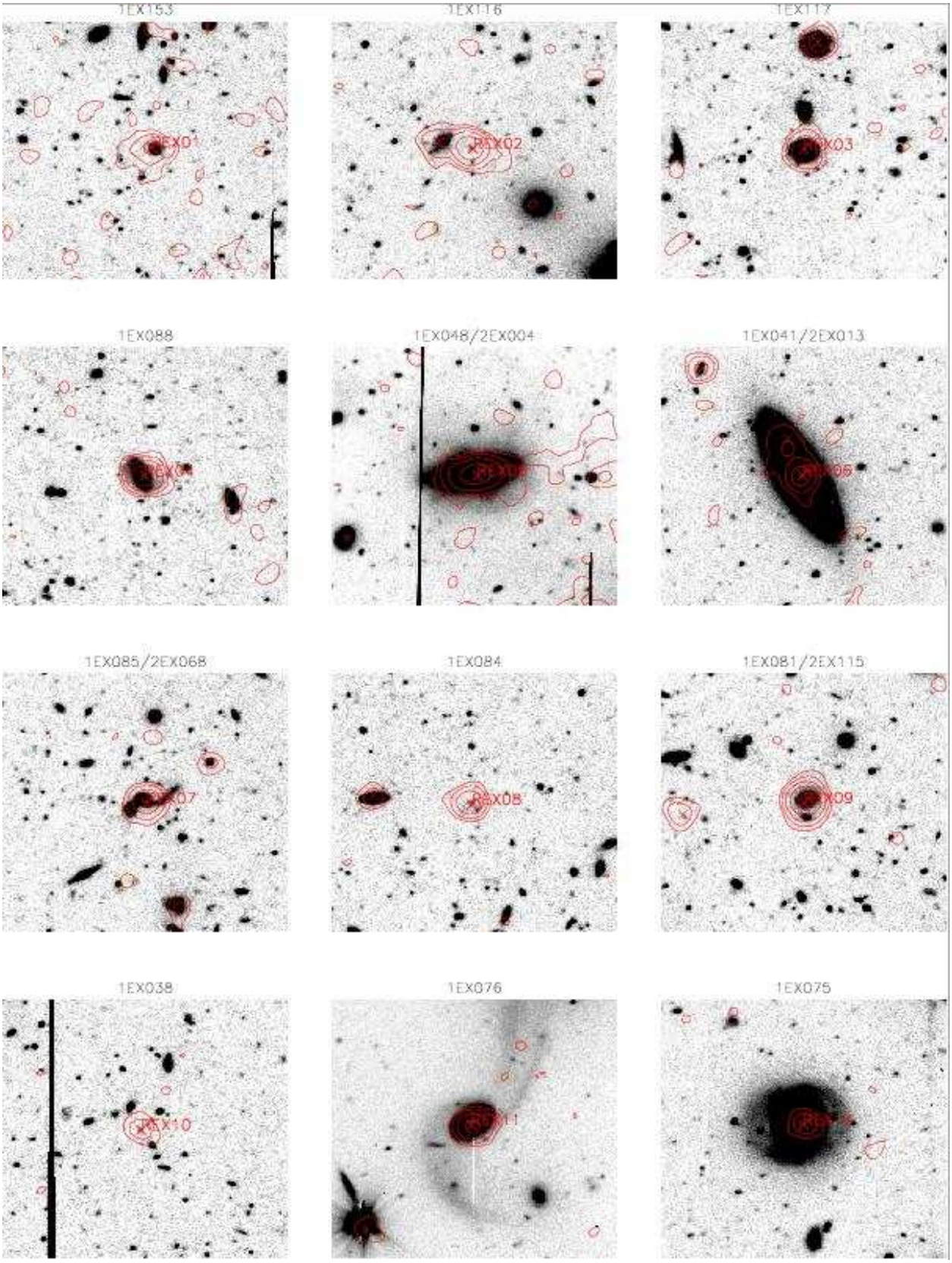

Fig. 7.— R-band images centered at the positions of the radio counterparts. The image size is $60'' \times 60''$. North is up, and east to the left. Red 1.4 GHz contours are plotted at a step of 2, 4, 8, 16, 32 $\times\sigma$. Crosses present the positions of the 1.4 GHz radio sources.

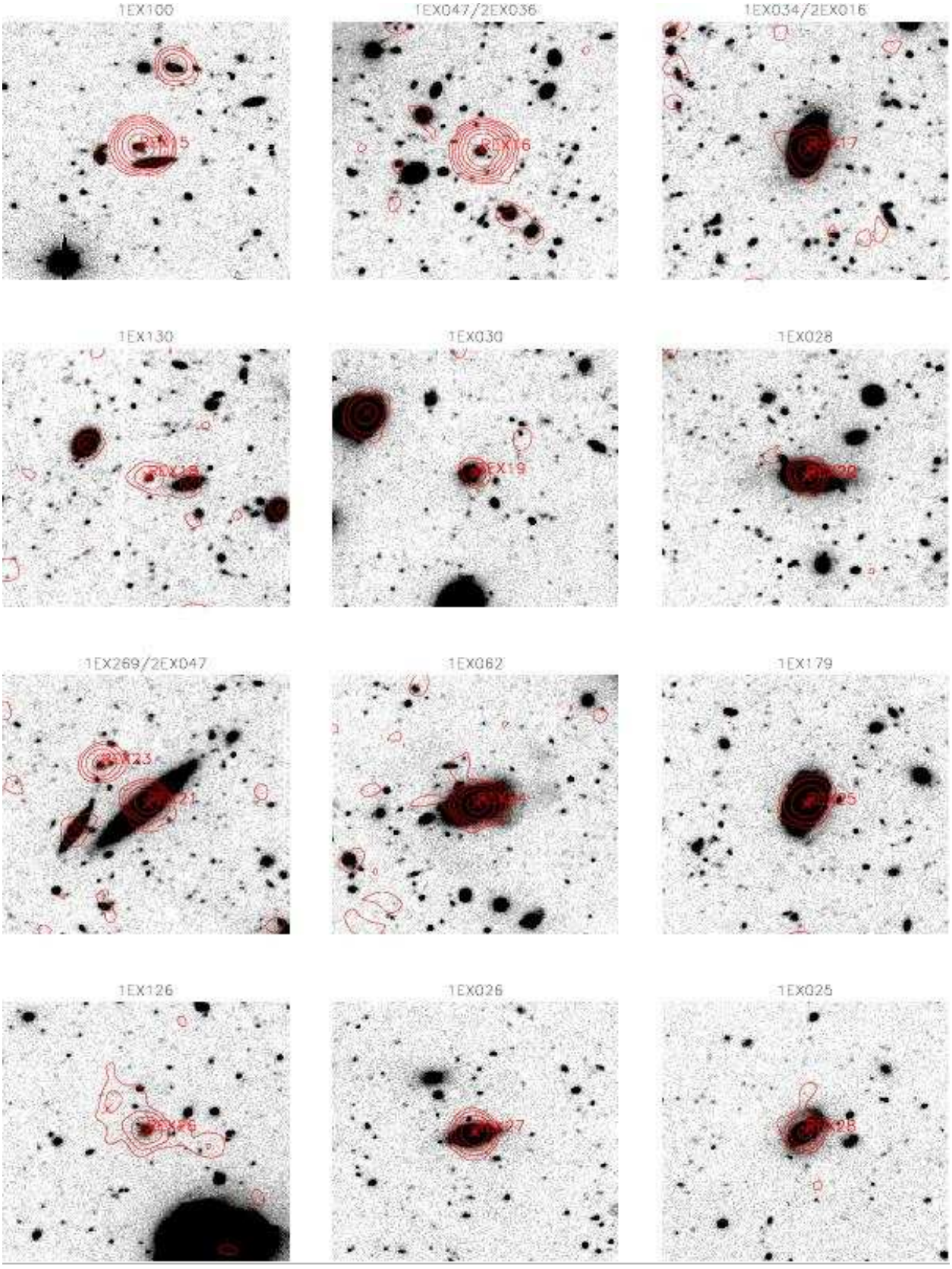

Fig. 7.— Continued

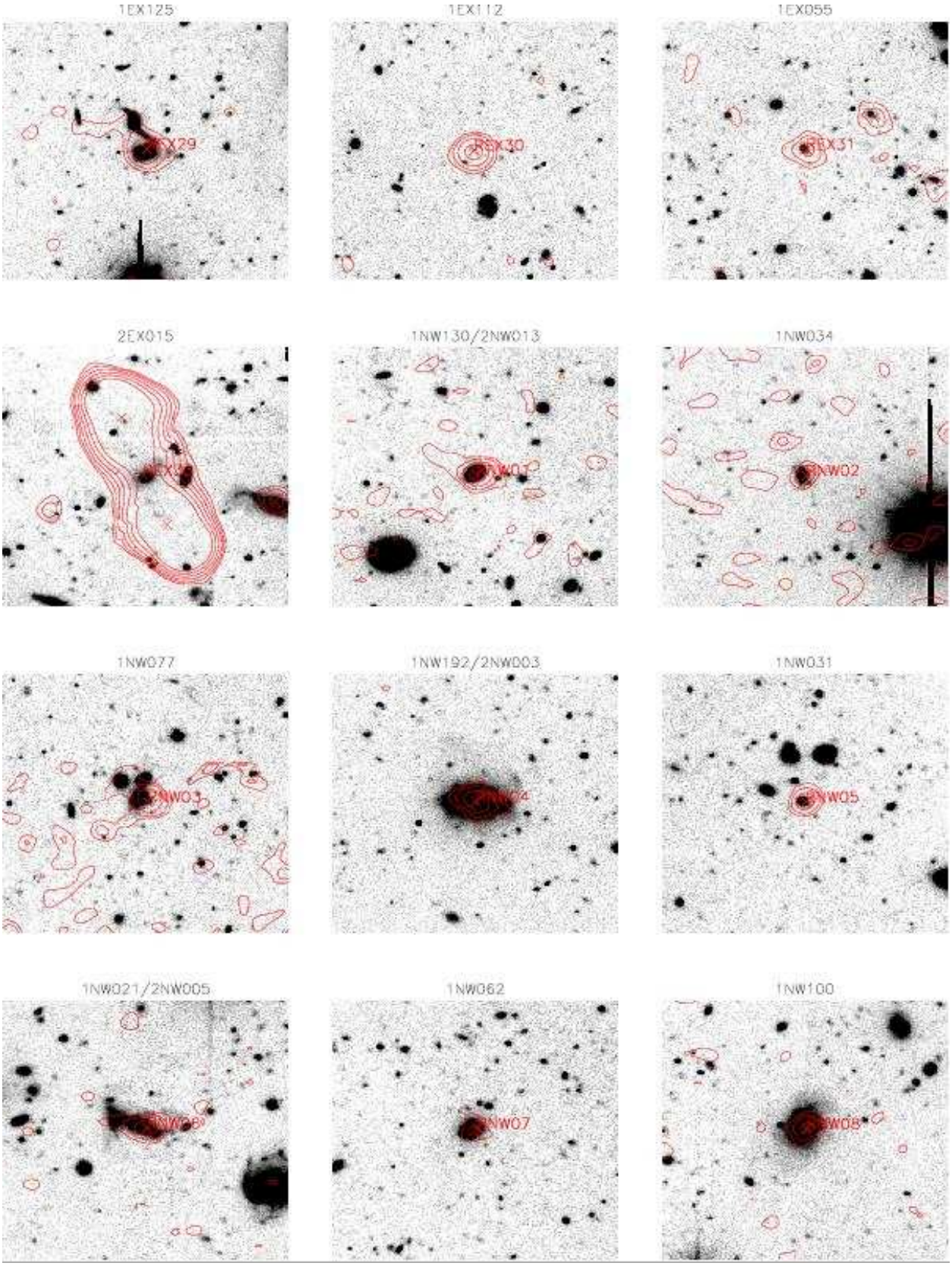

Fig. 7.— Continued

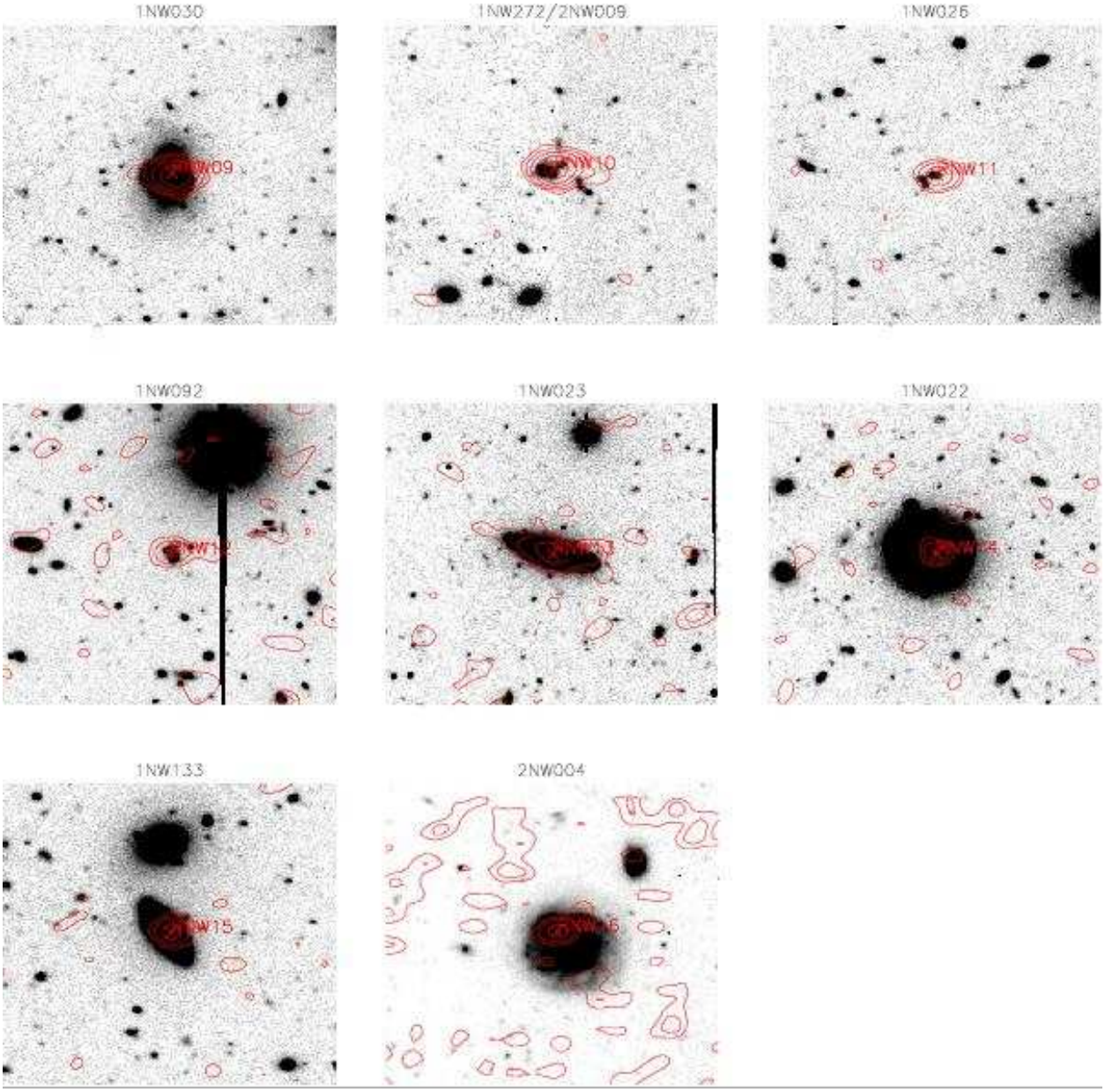

Fig. 7.— Continued

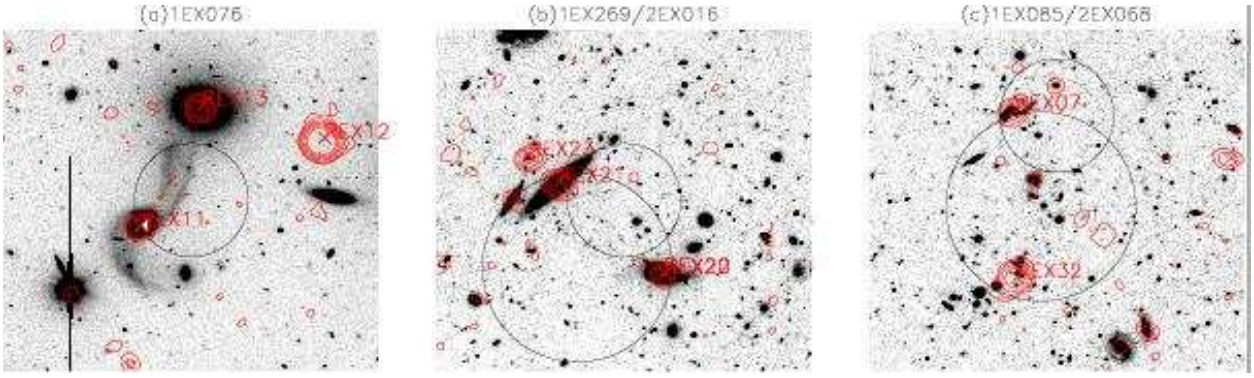

Fig. 8.— Wide R-band images($2' \times 2'$) for detail explanation of the identification of (a)1EX076, (b)1EX269/2EX016 and (c)1EX085/2EX068. Red Contours and crosses are same as Fig. 7. Small and large circles show 1σ positional error of the 90 μm sources and the 170 μm sources, respectively.

4. Discussion

4.1. Redshift and FIR Luminosity

Spectroscopic redshifts of 29 out of 44 FIR sources in Table 4 are available. Twenty five optical spectra of FIR sources were obtained with the KECK II and WIYN telescopes while redshifts of four objects (1NW062, 1NW100, 1NW092 and 1NW044) were kindly provided to us by A. Barger (private communication). The 25 optical spectra are shown in Figure 9.

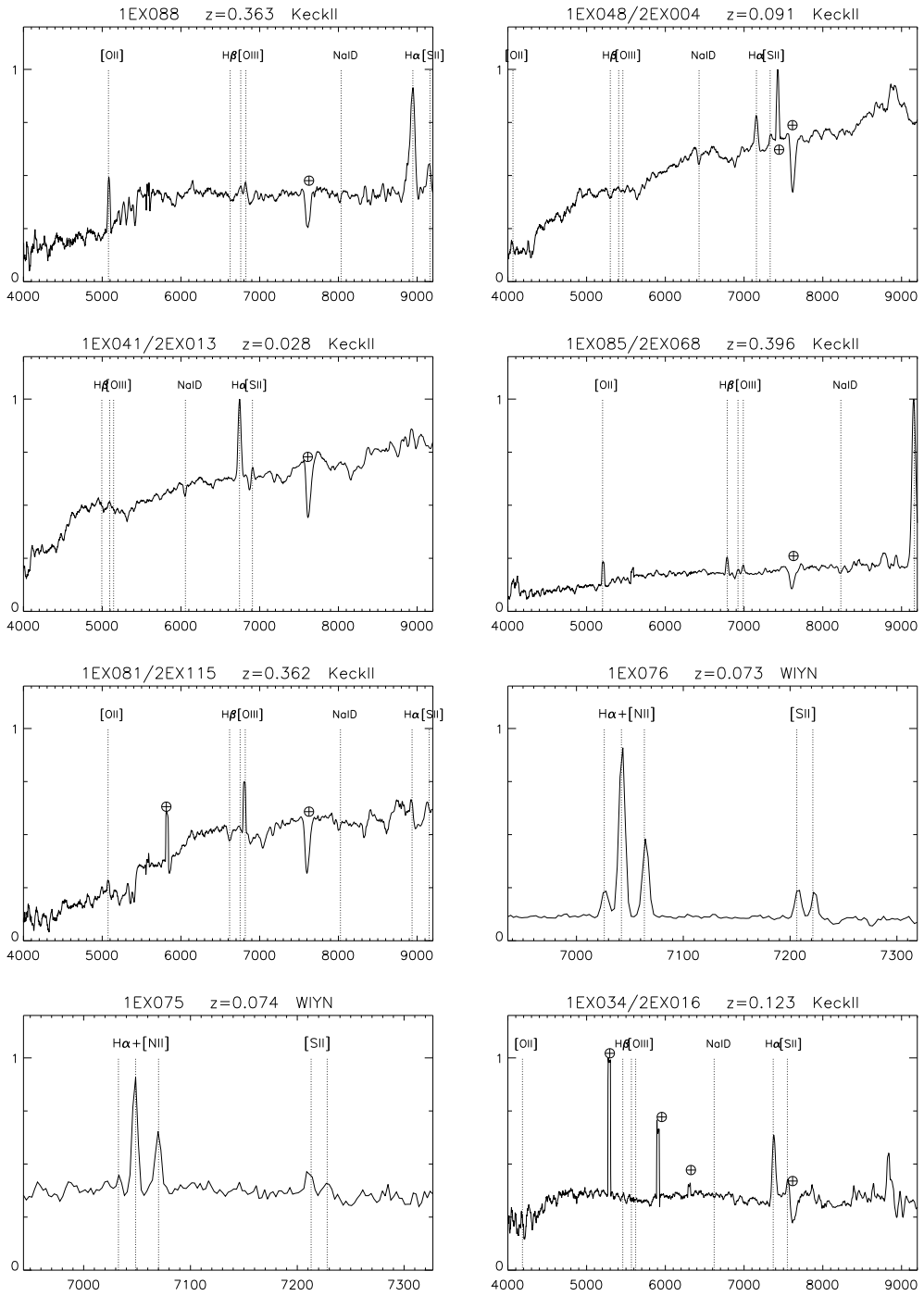

Fig. 9.— Optical spectra of *ISO* FIR sources. The wavelength is given in Ångstrom and vertical axis is an arbitrary unit. Regions with bad pixels, residuals of night sky emission and atmospheric absorptions are marked with ⊕.

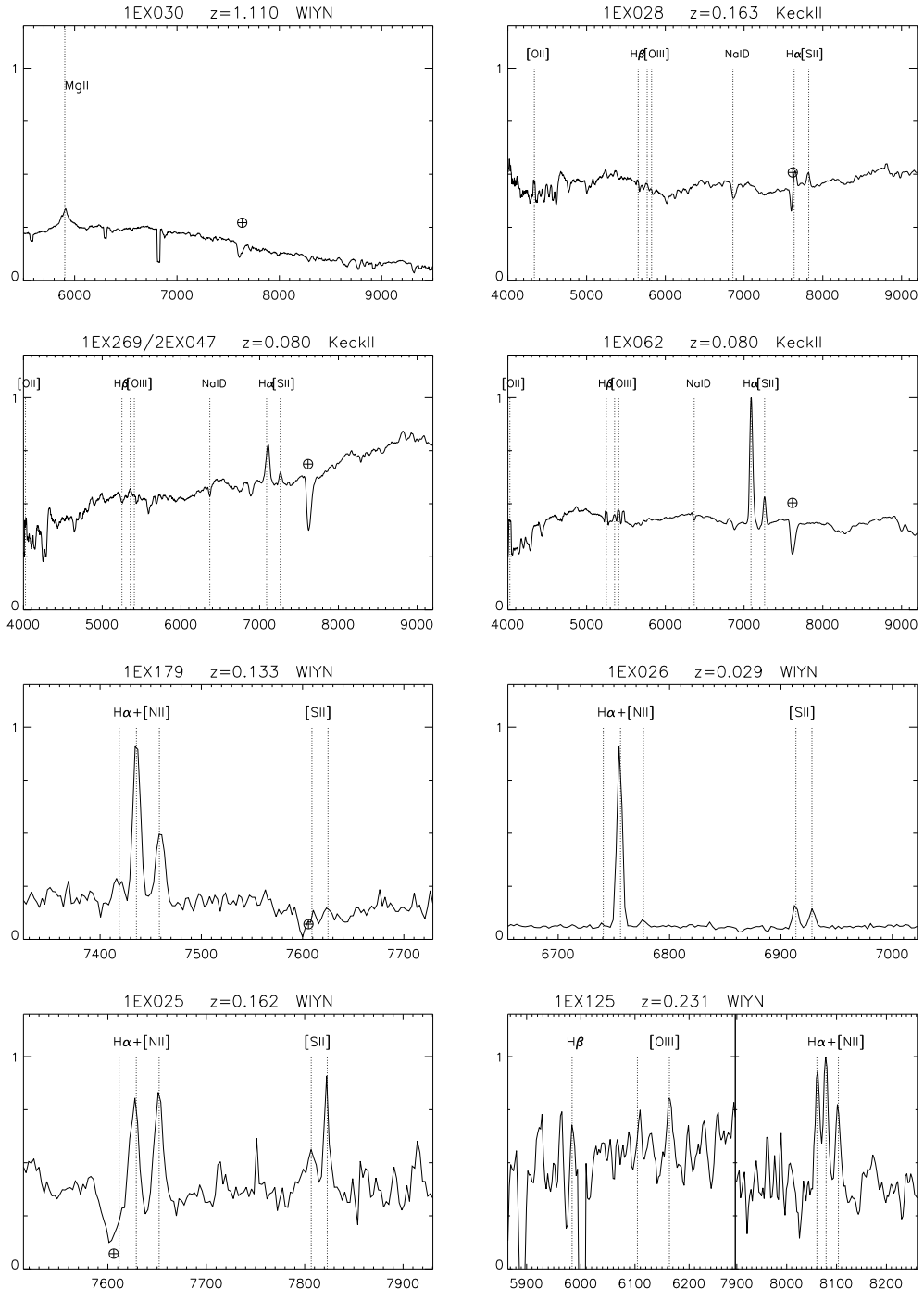

Fig. 9.— Continued

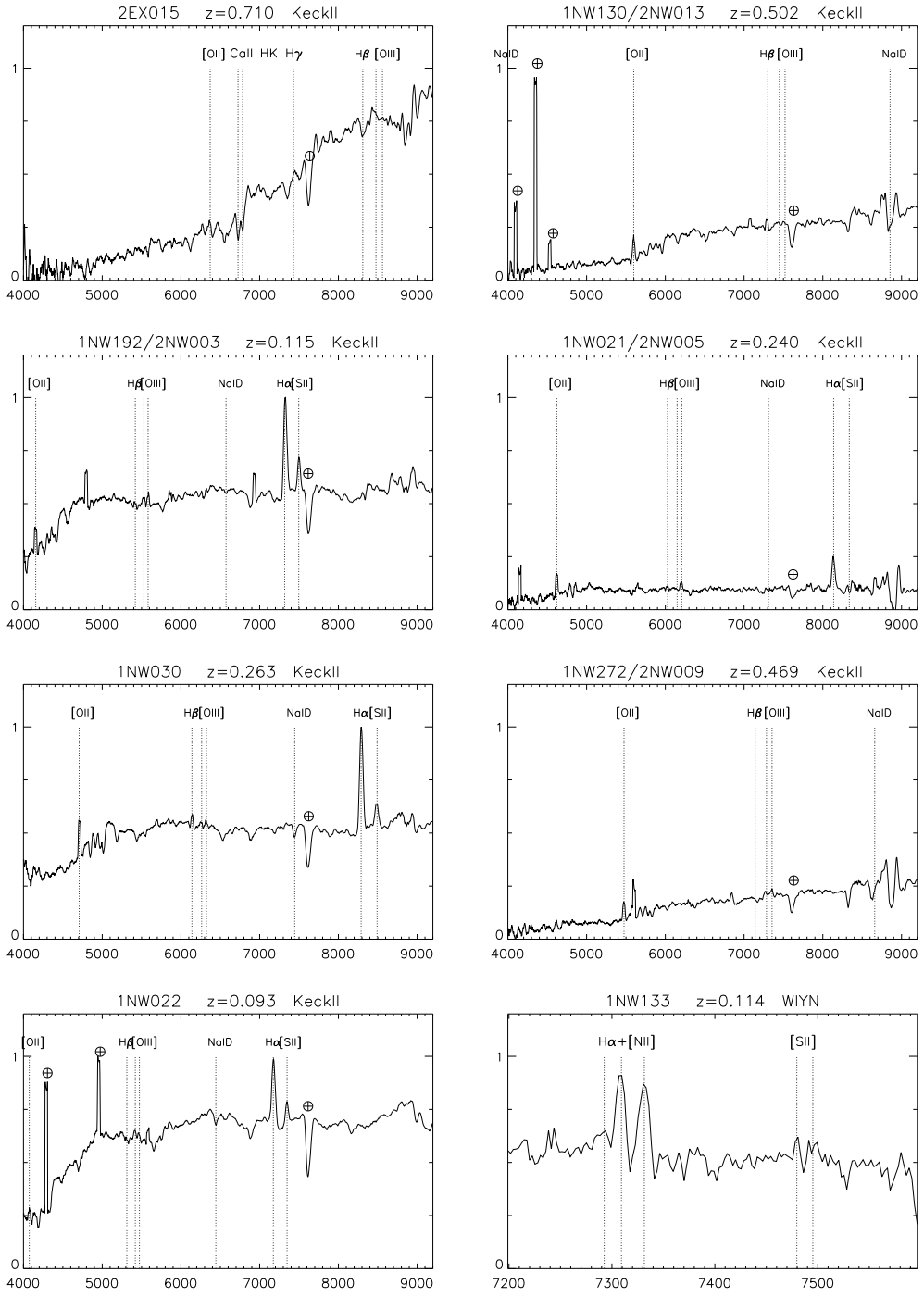

Fig. 9.— Continued

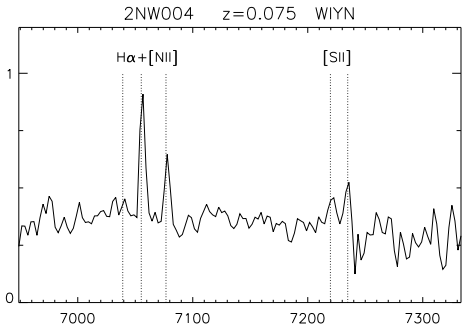

Fig. 9.— Continued

The redshift distributions of all FIR sources and 170 μm-detected FIR sources are shown in Figure 10 by open and filled histograms. Although more distant sources are expected at 170 μm than at 90 μm because of the strong k-correction brightening for dust emission, there are no significant differences in the redshift distribution between the sources detected at 170 μm and the sources detected only at 90 μm. Seven out of twelve (58%) 170 μm-detected source and nineteen out of twenty seven (70%) 90 μm-only-detected sources lie at $z < 0.3$. This may be attributed to the small number statistics. Patris et al. (2003) reported that 95% (20/21) of 170 μm sources brighter than 200 mJy found in their FIRBACK southern Marano fields are at $z < 0.3$. Our 170 μm sources are slightly more distant than theirs although their flux limit and their cumulative number density down to this limit are similar to ours. Their radio survey is shallower using a larger observing beam, and these and other aspects of their source identification procedure might have introduced a bias toward optically bright foreground sources.

The redshift versus IR color relation is plotted in Figure 11 for our *ISO* FIR sources together with expectation from greybodies with λ^{-1} and λ^{-2} emissivities at $z = 0 - 10$. Most of *ISO* FIR sources with 170 μm detection have a dust temperature ranging from 20-30 K for λ^{-1} and 15-25 K for λ^{-2}, which is consistent with the 170 μm/90 μm color temperature distribution of 74 ELAIS sources reported by Héraudeau et al. (2004).

The FIR flux, $F_{FIR}(40\mu\mathrm{m} - 500\mu\mathrm{m})$, can be estimated from the gray body fitting with the observed $F^C(90\mu m)$ and $F^C(170\mu m)$, the temperature from Figure 11 and the assumption of λ^{-2} emissivity. Adopting the different dust emissivity, λ^{-1}, the FIR flux, F_{FIR}, increase 15 percents on average. This assumption will not change the main conclusion of this paper. It should be noted that the detection limits (43 mJy at 90 μm and 102 mJy at 170 μm after the correction for the flux bias) are substituted into the undetected band for the objects detected only in one band.

The FIR luminosity, L_{FIR}, is then obtained as,

$$L_{FIR} = 4\pi D_L^2 \times F_{FIR}, \tag{13}$$

where D_L is the luminosity distance. The resultant FIR luminosity is given in Table 4 and plotted in Figure 12 as a function of redshift. Our sample consists of 24 sources with $L_{FIR} < 10^{12}\mathrm{L}_\odot$, four with $L_{FIR} = 10^{12-13}\mathrm{L}_\odot$, and one with $L_{FIR} > 10^{13}\mathrm{L}_\odot$. In the *IRAS* bright source catalog, only six out of 324 sources have $L_{FIR} > 10^{12}\mathrm{L}_\odot$ (Soifer et al. 1987). Thus, a fraction of $L_{FIR} > 10^{12}\mathrm{L}_\odot$ sources are 10 times greater in our *ISO* sample than in the IRAS bright source catalog. All the *IRAS* bright sources lie within $z \leq 0.1$, while, only 10 of 29 sources are at $z \sim 0.1$ in our *ISO* sample. It is noted here that our spectroscopy project is not complete yet, and all the sources with $L(90\mu\mathrm{m})/L(R) > 50$ are left unobserved. It is generally agreed that sources with $L(90\mu\mathrm{m})/L(R) > 50$ belong to a population of ULIRGs with $L_{FIR} > 10^{12}\mathrm{L}_\odot$. Hence, our sample should contain a greater fraction of $L_{FIR} > 10^{12}\mathrm{L}_\odot$ sources than that derived from our current spectroscopic knowledge.

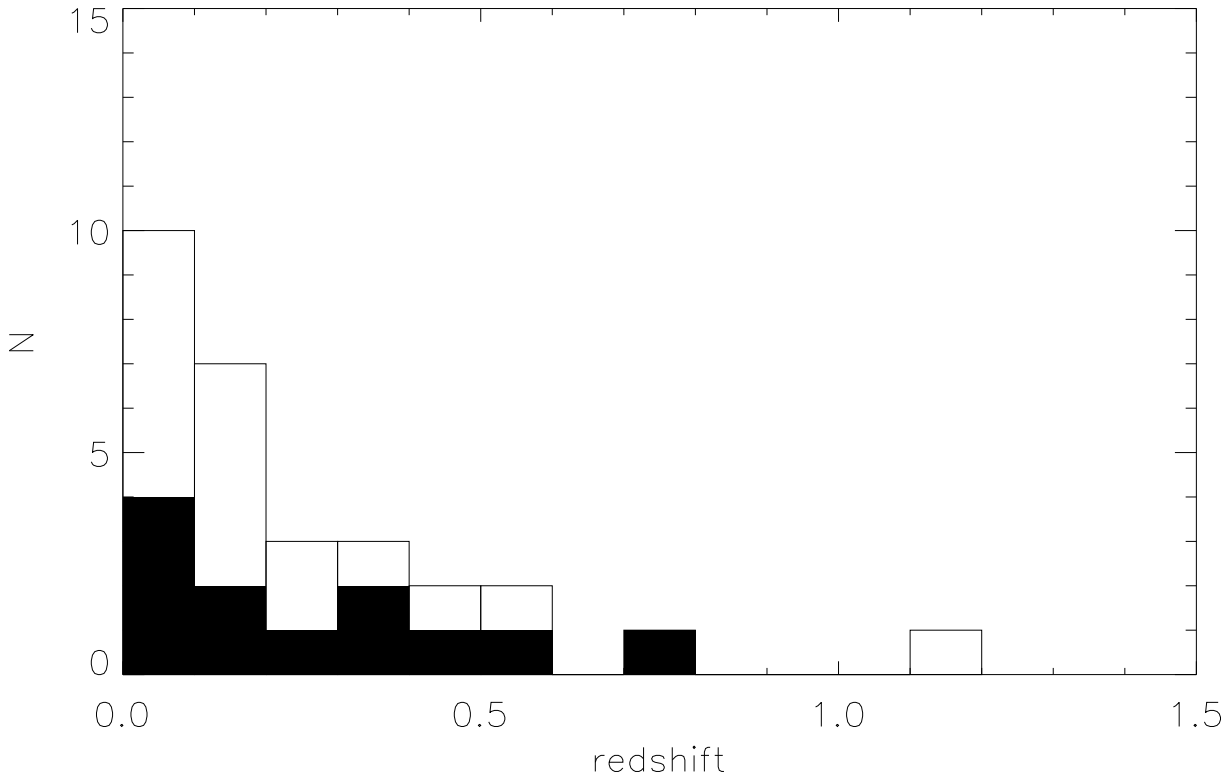

Fig. 10.— Redshift distributions of *ISO* FIR sources in the Lockman Hole. The open histogram show all the sources while the shaded histogram plots the 170 μm detected sources.

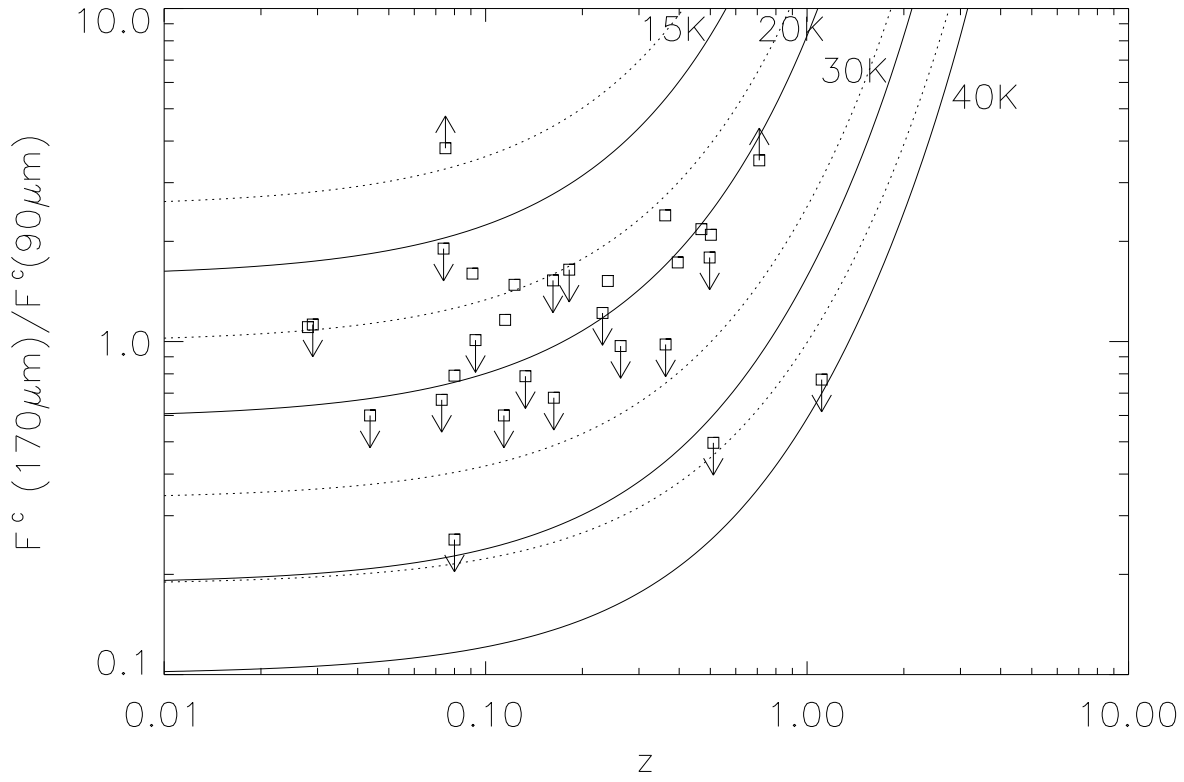

Fig. 11.— Relation of redshift versus flux ratio, $F^C(170\mu\mathrm{m})/F^C(90\mu\mathrm{m})$. Solid and dotted lines show the expectation from a single temperature blackbody multiplied by an $\lambda^{-\beta}$ emissivity. The calculations are made for temperatures of 15K, 20K, 30K and 40K. Solid lines plot the flux ratios for an λ^{-2} emissivity, and dashed lines an λ^{-1} emissivity.

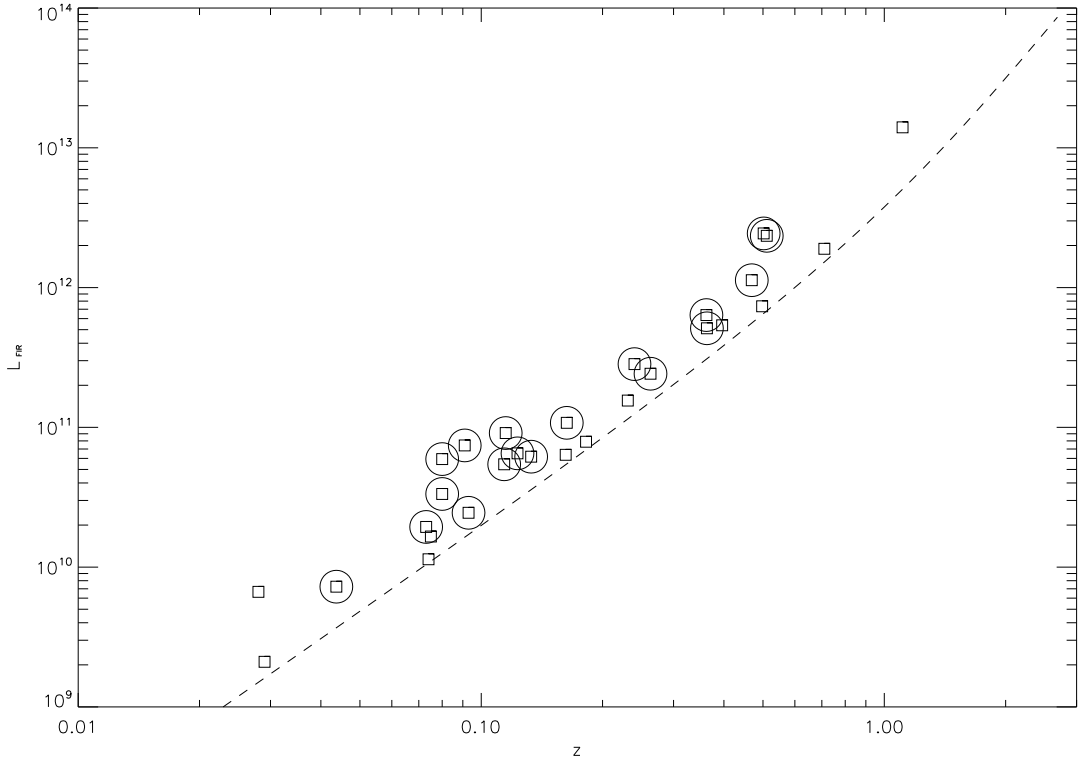

Fig. 12.— Relation of L_{FIR} versus redshift. Squares with no circle denote sources which are not used to derive the luminosity function of ISO FIR sources, because they are either too faint or outside the redshift bins. The dashed line presents our detection limits of the ISO FIR observations.

4.2. Luminosity functions

Here we derive luminosity functions of our *ISO* FIR sources having $F^C(90\mu\mathrm{m}) \geq 85$ mJy. These new criterion is more strict than those used to identify sources having $F^C(90\mu\mathrm{m}) \geq 43$ mJy or $F^C(170\mu\mathrm{m}) \geq 102$ mJy. The reason for using the new criteria is to control the detection limit of our *ISO* FIR sources simply and to avoid from the large correction for the completeness of the sample. 27 out of 44 galaxies identified with *ISO* FIR sources meet the new criterion, and their redshifts of 21 sources are available.

The luminosity function, $d\Phi(L_{FIR})/dL_{FIR}$, (i.e., the volume density of galaxies per unit luminosity range) is derived by following the the $1/V_{max}$ method as described in Schmidt (1968) and Eales (1993). The volume density of galaxies with luminosity between L and $L + dL$ is defined as,

$$\frac{d\Phi(L_{FIR})}{dL_{FIR}} dL_{FIR} = \sum_j \frac{1}{p(F^C)V_j}, \tag{14}$$

where $p(F^C)$ is the detection probability for source with corrected flux F^C, and the summation is over all sources with luminosity between L and $L + dL$ in the sample. $p(F^C)$ is obtained by combining the detection rate given in Figure 3 by Kawara et al. (2004) with Equ. (1) for transforming the observed flux F to the corrected F^C. V_j is defined as,

$$V_j = \int_\Omega \int_{z_{min}}^{z_{max}} \frac{d^2V}{d\Omega dz} dz d\Omega. \tag{15}$$

where Ω is the solid angle in this survey and $d^2V/d\Omega dz$ is the comoving volume element. z_{max} is the maximum redshift defined by the limiting fluxes at the faintest end, namely, $F^C(90\mu\mathrm{m}) = 85$ mJy, while z_{min} is the minimum redshift by the flux limits at the brightest end which is set to 1 Jy for 90 μm. The luminosity functions are derived for three redshift bins; $z = 0.03 - 0.10$, $z = 0.10 - 0.30$ and $z = 0.30 - 0.60$. These redshift bins correspond to the different FIR luminosities, $L_{FIR} = 0.7 - 7.4 \times 10^{10} \mathrm{L}_\odot$, $L_{FIR} = 5.4 - 28 \times 10^{10} \mathrm{L}_\odot$, and $L_{FIR} = 51 - 240 \times 10^{10} \mathrm{L}_\odot$, respectively.

Table 5. Luminosity function of *ISO* FIR sources.

	$z = 0.03 - 0.10$	$z = 0.10 - 0.30$	$z = 0.30 - 0.60$
L_{FIR} $[10^{10} L_\odot]$	0.7-7.4	5.4 - 28	51 -240
N[a]	6	7	5
$\frac{d\Phi}{d\log L}$[b] $[\mathrm{Mpc}^{-3}\ \mathrm{dex}^{-1}]$	$(1.9 \pm 0.9) \times 10^{-3}$	$(4.6 \pm 1.3) \times 10^{-4}$	$(4.6 \pm 1.3) \times 10^{-5}$

[a]The number of objects used to derive the space densities.

[b]Error is from the Poisson statistics.

This reason is that the luminosity of the *ISO* FIR sources is following as a function of redshift (See Fig. 12). The numbers of objects in each bin are 6, 7 and 5 and three sources which have $F^C(90\mu\mathrm{m}) \geq 85\mathrm{mJy}$ are out of these three bins: two of them are at $z < 0.03$ and the other is at $z = 1.1$. The luminosity function requires the following additional conditions; $z_{max} = z_u$ for $z_{max} > z_u$ and $z_{min} = z_l$ for $z_{min} < z_l$ where z_u and z_l are the maximum and minimum redshifts of the specific redshift bin.

The luminosity function of our *ISO* FIR sources sample is given in Table 5. Figure 13 compares the *ISO* FIR sources sample with other galaxy samples. These result is calculated by summing up $1/p(F^C)V_j$ of the sources having the redshift(Equ. (14)). Our spectroscopic redshifts are obtained for 78%(21/27) of this sample and no correction by a factor of 1.3 (27/21) was not applied in Table 5 and Figure 13. The six *ISO* FIR sources without redshift are not expected to be the same populations as our 21 *ISO* FIR sources having redshift, because the six sources without redshift tend to have higher $L(90\mu\mathrm{m})/L(R)$ than those in redshift-measured source; sources without redshift have the range $30 < L(90\mu\mathrm{m})/L(R) < 1400$, while the 20 redshift-measured sources have $1 \lesssim L(90\mu\mathrm{m})/L(R) \lesssim 20$ and one source at z= 0.469 have $L(90\mu\mathrm{m})/L(R) = 43.7$.

The comparison includes the *IRAS* bright galaxy sample by Soifer et al. (1987) with the mean redshift of $< z > \sim 0.04$, the *IRAS* 1Jy ULIRG sample by Kim & Sanders (1998) with $< z > \sim 0.15$, and the SCUBA galaxy sample by Barger, Cowie & Richards (2000) at $z = 1 - 3$. Here we assume that the infrared luminosity, $L_{IR}(8 - 1000\mu\mathrm{m})$, is nearly equal with the FIR luminosity, Ł$_{FIR}(40 - 500\mu\mathrm{m})$. The comparison shows a clear trend of the evolutionary effect; at a given luminosity, a greater density of galaxies for a higher redshift. It is particularly clear that there are a rapid evolution in the ULIRG population toward high redshift; the space densities are 1×10^{-7} Mpc^{-3} at $< z > \sim 0.04$ (Soifer et al. 1987), 5×10^{-7} Mpc^{-3} at $< z > \sim 0.15$ (Kim & Sanders 1998), and 4.6×10^{-5} Mpc^{-3} at $z = 0.3 - 0.6$. In other words, relative to the local universe, the space densities are ~ 5 times greater at $< z > \sim 0.15$ and ~ 460 times greater at $z = 0.3 - 0.6$. At the highest end of the FIR luminosity, the space densities are 1000 times greater at $z = 1 - 3$ than the local Universe.

There is uncertainty of flux calibration of our *ISO* FIR sources. Our flux calibration was done with one IRAS source(UGC 06009) which have ~ 50 percent flux errors(Kawara et al. 2004). This uncertainty brought systematic luminosity shift to 0.3 dex in Figure 13. However even if there were the 0.3 dex shift to lower luminosity, the evolution of *ISO* FIR sources, especially at $z = 0.3 - 0.6$ still exists. In addition, we compared the 90 μm luminosity function of the ELAIS(Serjeant et al. 2004). Serjeant et al. (2004) presents that the *ISO* 90 μm luminosity function of the ELAIS is consistent with the IRAS with the assumption of pure luminosity evolution of $(1 + z)^3$. If we apply their pure luminosity evolution of $(1 + z)^3$ in our data, at least our luminosity function at $z = 0.03 - 0.1$ and $0.1 - 0.3$ are consistent with that of ELAIS and IRAS Bright galaxy sample. On the other hand, the luminosity function at $z = 0.3 - 0.6$ show an luminosity excess by a factor of $\sim$2 of that of IRAS Bright galaxy sample after luminosities reduced by a factor of $(1 + z)^3$. This suggests much stronger evolution to the *ISO* FIR sources at this redshift range where ELAIS can

barely observe. It is noted again that our spectroscopic observations miss almost all sources with $L(90\mu\mathrm{m})/L(R) > 30$, many of which would belong to a population of ULIRGs with $L_{FIR} > 10^{12}\mathrm{L}_{\odot}$. The space density of ISO FIR sources with $L_{FIR} > 10^{12}$,which is derived here, must be significantly underestimated.

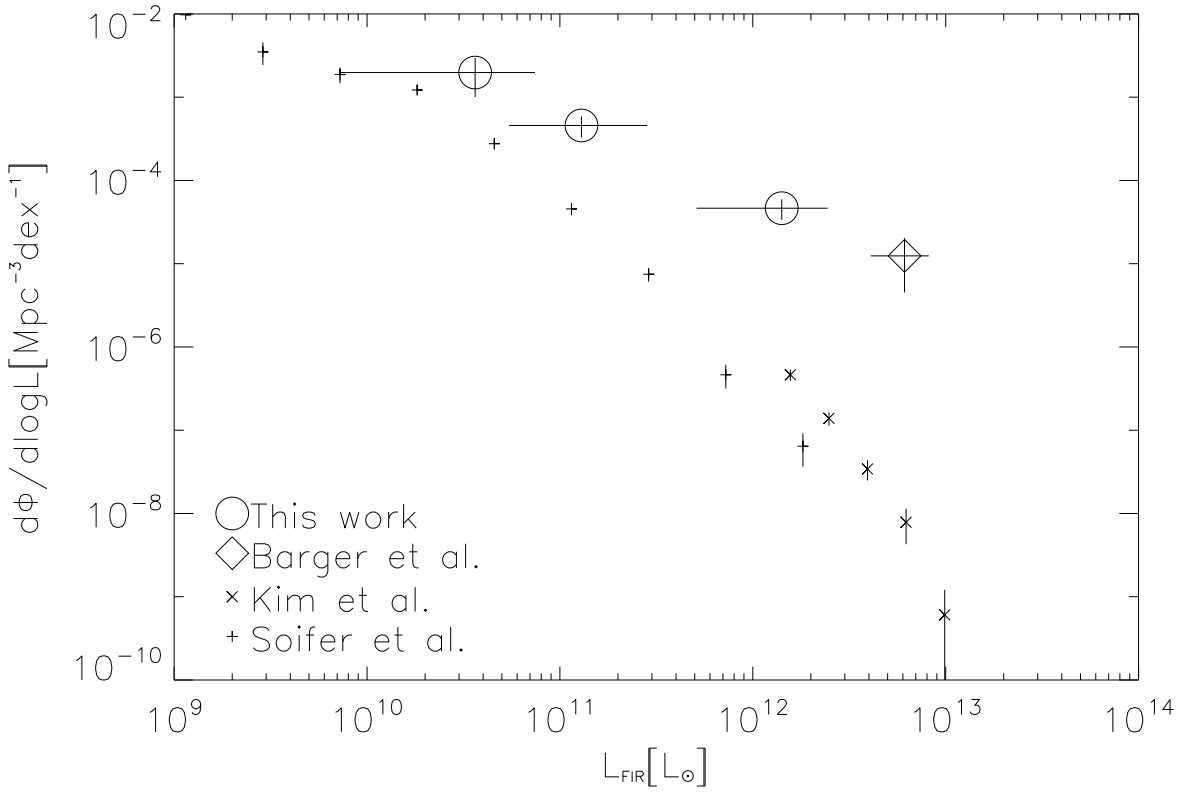

Fig. 13.— Comparison of the luminosity function (LF) of the *ISO* FIR source sample with other samples. Circles present the LF of the *ISO* FIR source sample which is plotted in the redshift bins; $z = 0.03 - 0.10$, $z = 0.10 - 0.30$ and $z = 0.30 - 0.60$ from left to right. Horizontal error bars represent the luminosity ranges of the sub-sample in the redshift bins and vertical error bars represent the Poisson errors. Pluses show the LF of the *IRAS* bright galaxy sample at $< z > \sim 0.04$ (Soifer et al. 1987), small crosses the *IRAS* 1Jy ULIRG sample at $< z > \sim 0.15$ (Kim & Sanders 1998), and diamonds the SCUBA source sample at $z = 1 - 3$ (Barger, Cowie & Richards 2000). In order to present the data of Soifer et al. (1987), Kim & Sanders (1998) and Barger, Cowie & Richards (2000), the infrared luminosity, L_{IR}, is assumed to be L_{FIR}.

4.3. Nature of *ISO* FIR sources

The fraction of *ISO* FIR sources associated with an AGN is estimated from optical emission lines, radio continuum emission, and X-ray activity. The excitation diagnosis by Veilleux & Osterbrock (1987) is applied to the spectra of the *ISO* FIR sources for the optical spectral classification. One object (1EX030) is a quasar with $L_{FIR} = 10^{13.1} L_{\odot}$ at $z = 1.11$. Two objects (1EX025 & 1NW133) are type II Seyferts or LINERs with $L_{FIR} = 10^{10.8-10.9} L_{\odot}$ at $z = 0.11 - 0.16$. Two objects (1EX026 & 1EX076) are HII galaxies with $L_{FIR} = 10^{9.4-10.4} L_{\odot}$ at $z = 0.03 - 0.07$. The remaining galaxies are left unclassified because of the insufficient wavelength coverage, spectral resolution, or quality of the spectrum. Optical images indicate that four galaxies and possibly another two are interacting systems. Their optical properties are summarized in Table 4.

The relationship between 1.4 GHz and FIR emission is examined on the $L(1.4GHz)/L(90\mu\mathrm{m})$ versus $F^C(170\mu\mathrm{m})/F^C(90\mu\mathrm{m})$ diagram as shown in Figure 14[5]. Open and filled squares represent sources lying in the LHEX and LHNW fields, respectively. The dashed and dotted lines are the redshift loci of two different types of ULIRGs, NGC 6240 (with an AGN) and Arp 220 (without an AGN) (e.g. Smith et al. 1998), while the dash dotted line shows that of starburst galaxy M82. This figure indicates that most of the *ISO* FIR sources are pure star forming or star-formation dominated galaxies as they lie near the loci of Arp 220 and M82. Three optically classified AGNs, 1EX030, 1EX025 & 1NW133, also appear in the same area occupied by star-formation dominated objects. Three FIR sources, 1EX100, 1EX047/2EX036, and 1NW272/2NW009, are found near the locus of NGC 6240. 1NW272/2NW009 is classified as type II AGN with $L_{FIR} = 10^{12.2} L_{\odot}$ at $z = 0.47$. No spectroscopic data are available for the two other sources. The source 2EX015, which has the highest $L(1.4GHz)/L(90\mu\mathrm{m})$, is identified with a powerful radio galaxy at $z = 0.710$.

As discussed so far, our sample contains at least seven galaxies hosting an AGN and five ULIRGs. Three AGN-host galaxies have FIR luminosity characteristic of ULIRGs. Thus, 60% (3/5) of our ULIRGs are AGN galaxies, in agreement with that found in the IRAS sample (Sanders & Mirabel 1996), and this suggests that the fraction of AGN galaxies with the ULIRG luminosity does not change much from the local Universe to $z \sim 0.5$. The deep X-ray survey have been conducted in the LHEX field by ROSAT and XMM-Newton satellites (e.g. Lehmann et al. 2001; Mainieri et al. 2002). If our seven AGNs have the X-ray to FIR luminosity ratio L_X/L_{FIR} similar to those of AGN-associated ULIRGs such as NGC 6240 and Mrk 231, 2×10^{-15} erg cm^{-2} s^{-1} and 6×10^{-15} erg cm^{-2} s^{-1} are expected at the 0.5-2 keV and 2-10 keV energy bands, respectively, for objects having 100 mJy at 100 μm. Out of our seven AGN galaxies, only one source, 1EX030, identified as a quasar, has been detected in the X-ray. Two undetected sources lie within the ROSAT deep survey area with a flux limit of 10×10^{-15} erg cm^{-2} s^{-1}, and it is not surprising that these galaxies were not detected by ROSAT. The powerful radio galaxy 2EX015 at $z = 0.710$ and another AGN candidate 1EX110 (which has no optical spectrum yet) are found within the XMM-

[5] $L(1.4GHz)$, $L(90\mu\mathrm{m})$ and $L(R)$ are monochromatic luminosities and are defined by $4\pi D_L^2 \nu f_\nu$ where D_L denotes the luminosity distance to the object.

Newton survey area with a limiting flux of 1.4×10^{-15} erg cm^{-2} s $^{-1}$ in the 2-10 keV energy bands. The X-ray non-detection of these two objects may be attributed to a Compton thick absorber with a column density of 3×10^{24} cm^{-2}, which is equivalent to $A_V \sim 1200$ mag. The two remaining AGN sources are outside the X-ray survey area. It is interesting that the fraction of AGN host galaxies detected by the deep X-ray surveys is rather small. This is also a nice demonstration that the combination of FIR and radio observations offers a powerful tool to find heavily obscured AGNs which might be difficult to be found in the X-ray.

The 90 μm luminosity relative to the optical R-band luminosity, $L(90\mu\mathrm{m})/L(R)$, is plotted against optical color , $R-I$, in Figure 15. Two large symbols (square and diamond) are FIRBACK 170 μm sources, FN1-40 at $z = 0.449$ and FN1-64 at $z = 0.907$ (Chapman et al. 2002). The loci expected from the SEDs of NGC 6240, Arp 220, and M82 at $z = 0 - 2$ are shown using dashed and dotted lines. This figure demonstrates that the ISO succeeded in detecting objects with a wide range of $L(90\mu\mathrm{m})/L(R)$ ratio, from 1 to 1000, and show a bimodal distribution of $L(90\mu\mathrm{m})/L(R)$ for our ISO FIR sources. One peak with $1 < L(90\mu\mathrm{m})/L(R) < 3$ appears to represent the population of normal star forming galaxies in nearby universe because of their brightness in the optical. The other peak with FIR excess represents infrared dominant sources like Arp 220 whose luminosity is nearly entirely reprocessed by dust. In Rodighiero et al. (2005) which reduced same ISO data in the LHEX and made identification with radio and 15 μm sources(See Appendix for details), nine of 11 sources were fitted with the SEDs of M82 or M51 which are FIR moderate galaxies, while two others have a Arp 220 SED. The number of Arp 220-like sources seem to be small, however their SED-template fitting was done for the sources whose redshifts are available. Thus there might be a bias to optically bright sources.

Figure 15 also shows that there is possibly a third class of objects with an extreme excess of FIR luminosity, $L(90\mu\mathrm{m})/L(R) > 500$. Although ULIRGs are known to have the largest intrinsic excess of the FIR luminosity relative to the optical luminosity, their extreme optical and FIR colors cannot be adequately explained by simply redshifting the observed SEDs of ULIRGs or starburst galaxies. Therefore, the five such objects, one from FIRBACK and four from our survey, may represent a new population of extreme FIR-excess galaxies. If the extreme values of $L(90\mu\mathrm{m})/L(R)$ are intrinsic, the small optical luminosity may imply that their stellar system has not been fully developed or their entire stellar structures are heavily obscured by dust.

Four such objects in the Lockman Hole fields are located on the outside of the field where the submillimeter and millimeter observations with the SCUBA, Bolocam and MAMBO(Scott et al. 2002; Greve et al. 2004; Laurent et al. 2005) were performed. In future, the measurements in such wavelength will give the additional information to them. In addition, one of the Spitzer Space Telescope Legacy Programs, SWIRE(Lonsdale et al. 2003), cover these fields in the wavelength from 3.6 μm to 160 μm and will release their data and help to understand four such objects.

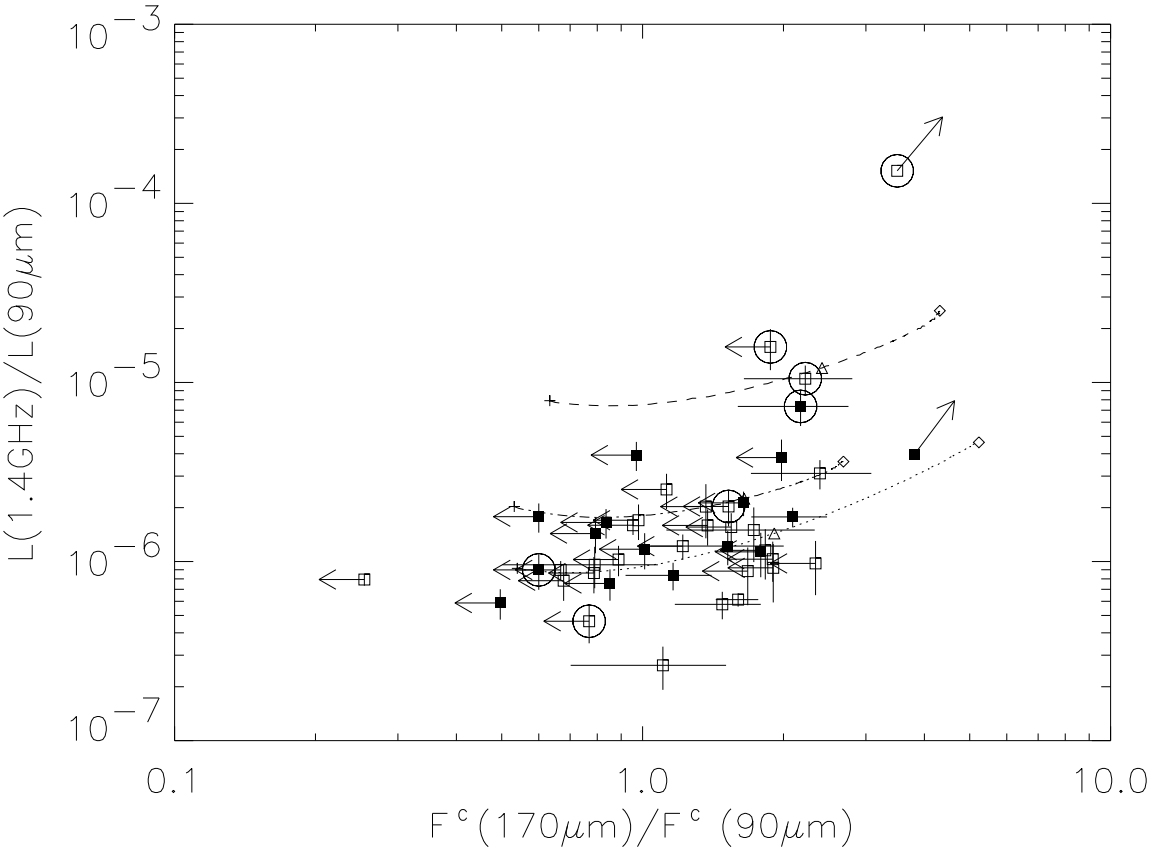

Fig. 14.— Relation of $F^C(170\mu m)/F^C(90\mu m)$ versus $L(1.4GHz)/L(90\mu m)$. Open squares show sources in the LHEX field while filled squares present those in the LHNW field. Seven large circles indicate galaxies showing AGN signatures. Dashed, dotted and dash-dotted lines represent the loci of redshiftted SEDs of NGC 6240, Arp 220, and M82, respectively. The crosses, triangles, and diamonds on the loci indicate z=0, 1.0 and 2.0.

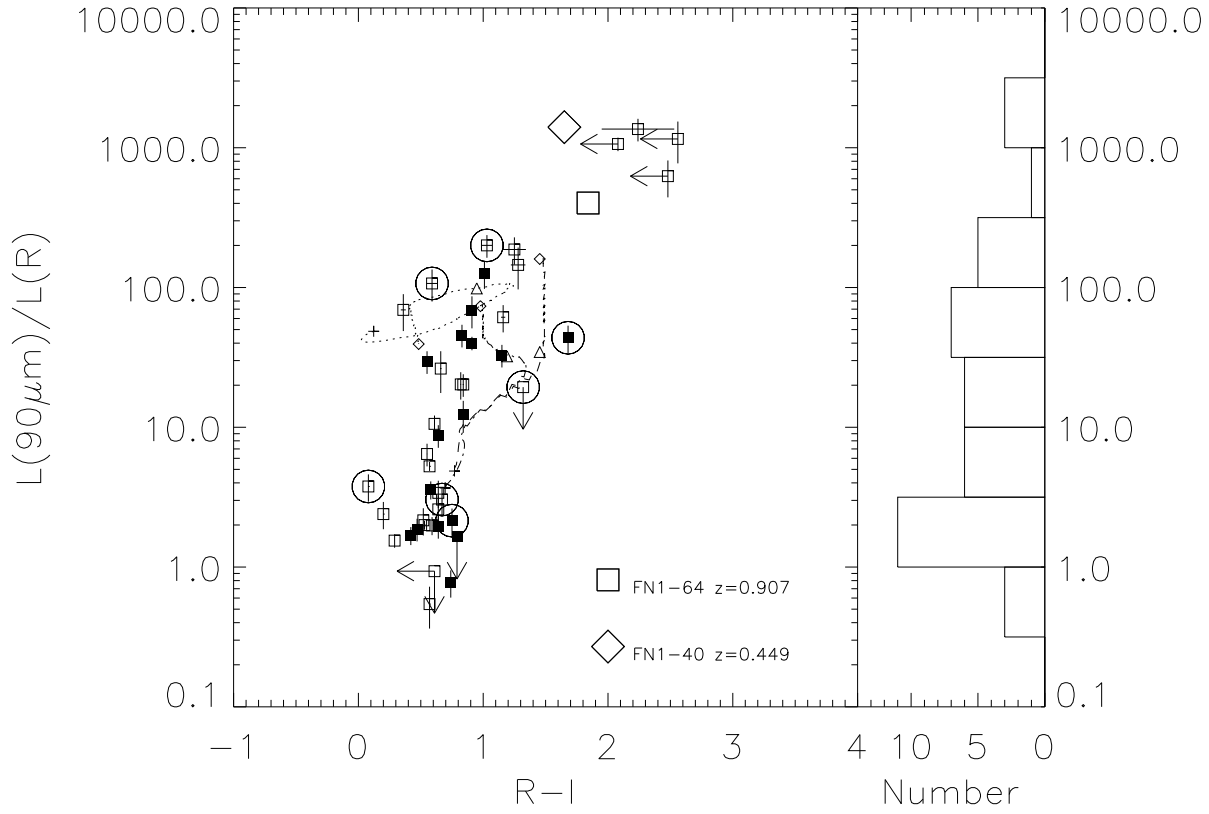

Fig. 15.— (left) 90 μm luminosity relative to the optical R-band luminosity plotted against optical $R-I$ color. Symbols are the same as in Figure 14 but with a large square and diamond which show the infrared luminous galaxies, FN1-40 and FN1-61, from the FIRBACK survey (Chapman et al. 2002). (right) The number distribution as a function of $L(90\mu m)/L(R)$ is shown to the right.

5. Summary

By exploiting the FIR-radio correlation, we have performed the Likelihood-Ratio analysis to identify the far-infrared sources that have been found in an area of ~ 0.9 deg^2 during the ISO deep far-infrared survey in the Lockman Hole. New observations have been conducted to construct the catalogs of radio and optical objects, which include a deep VLA 1.4 GHz observations, optical $R-$ & $I-$band imaging on the Subaru 8m and UH2.2m telescopes, and optical spectroscopy on the Keck II 10m and WIYN 3.5m telescopes. A summary of the results presented in this paper is as follows:

- Our samples of 116 and 20 sources are selected with the criteria of $F^C(90\mu\mathrm{m}) \geq 43$ mJy and $F^C(170\mu\mathrm{m}) \geq 102$ mJy, respectively. Our 1.4 GHz radio sample includes a total of 463 sources.

- In order to remove positional coincidence by chance, we calculate the Likelihood-Ratio and their reliability. As a results, 44 FIR sources are identified with radio sources.

- Optical identification of the 44 FIR/radio association is conducted using accurate radio positions. The dispersion in the difference between the radio and optical position is $0\farcs6$.

- Dust temperature derived from the FIR color ranges between 15 and 30 K.

- Spectroscopic redshifts have been obtained for 29 out of 44 identified sources. There are no significant differences in the redshift between 170 μm-detected sources and 90 μm-only-detected sources.

- 24 (out of 29) FIR galaxies with redshifts have $L_{FIR} < 10^{12}\mathrm{L}_\odot$, four with $L_{FIR} = 10^{12-13}\mathrm{L}_\odot$, and one $L_{FIR} > 10^{13}\mathrm{L}_\odot$.

- The luminosity functions are calculated using the $1/V_{max}$ method. The space density of the our sample galaxies at $z = 0.3 - 0.6$ is 4.6×10^{-5} Mpc^{-3}, which is 460 times as high as that at the local universe. A rapid evolution in the ULIRG population is suggested.

- Most of ISO FIR sources have $L(1.4GHz)/L(90\mu\mathrm{m})$ similar to star-forming galaxies Arp 220 and M82, indicating star formation is the dominant source of their FIR and radio emission in these galaxies.

- Our FIR sample contains at least seven AGNs, which are classified either from optical emission lines, excess in radio emission, or X-ray activity.

- 60%(3/5) of our ULIRGs are AGN galaxies, implying that the percentage of AGN galaxies with ULIRG luminosity does not change significantly between $z = 0$ and $z \sim 0.6$.

- Five of the seven AGN galaxies are within the ROSAT X-ray survey field, and two are within the XMM-Newton survey fields. X-ray emission has been detected in only one source, 1EX030,

which is optically classified quasar. If our AGN galaxies have L_X/L_{FIR} similar to NGC 6240, a ULIRG hosting an AGN, then none of our AGN galaxies would have been detected by ROSAT. The non-detection by XMM-Newton 2-10 keV band implies a very thick absorption column density of $3 \times 10^{24}\mathrm{cm}^2$ or $A_V \sim 1200$ mag obscuring the central source of the two AGN galaxies. The combination of FIR and radio observations would provide a powerful tool to find heavily obscured AGNs which might be difficult to be found in the X-ray.

- Several sources show an extreme FIR luminosity relative to the optical R-band, $L(90\mu\mathrm{m})/L(R) > 500$. Such extreme values cannot be explained from the redshifted SEDs of ULIRGs and may imply a new population of galaxies where an extreme activity of star formation in an undeveloped stellar system. If so, we might be looking at the formation of bulges or ellipticals.

We wish to thank the staff of the Subaru Observatory, NOAO, NRAO, Keck Observatory and the UH88 telescope for their assistance and hospitality during the several observing runs in which collected data for this paper. This research made use of the NASA/IPAC Extragalactic Database (NED) which is operated by the Jet Propulsion Laboratory, California Institute of Technology, under contract with the National Aeronautics and Space Administration. This paper is based on observations with *ISO*, an ESA project with instruments funded by ESA member states and with the participation of ISAS and NASA.

REFERENCES

Barger, A. J., Cowie, L. L., Sanders, D. B., et al., 1998, Nature, 394, 248

Barger, A.J., Cowie, L.L., & Richards, E.A., 2000, 119, AJ, 2092

Blain, A. W., Kneib, J.P., Ivison, R.J., & Smail, I., 1999, ApJ, 512, L87

Casali, 1992, UKIRT Newsletter, 4, 33

Chapman, S.C., Smail, I., Ivison, R.J., et al., 2002, ApJ, 573

Condon, J. J. 1992, ARA&A, 30, 575

de Ruiter, H. R., Arp, H. C., & Willis, A. G. 1977, A&AS, 28, 211

de Ruiter, H.R., Zamorani, G., Parma, P., et al., 1997, A&A, 319, 7

Eales, S., 1993, ApJ, 404, 51

Efstathiou, A., Oliver, S., Rowan-Robinson, M., et al., 2000, MNRAS, 319, 1169

Fadda, D., Lari, C., Rodighiero, G., Franceschini, A., Elbaz, D., Cesarsky, C., & Perez-Fournon, I. 2004, A&A, 427, 23

Fixsen, D.J., Dwek, E., Mather, J.C., et al. 1998, ApJ, 508, 123

Flores H. et al., 1999, ApJ, 517, 148

Fox, M.J., Efstathiou, A., Rowan-Robinson, M., et al., 2002, MNRAS, 331, 839

Franceschine, A., Aussel, H., Cesarsky, C.J., Elbaz,D., & Fadda, D., 2001, A&A, 378, 1

Greve, T. R., Ivison, R. J., Bertoldi, F., Stevens, J. A., Dunlop, J. S., Lutz, D., & Carilli, C. L. 2004, MNRAS, 354, 779

Hasinger, G., Burg, R., Giacconi, R., Schmidt, M., Trumper, J., & Zamorani, G. 1998, A&A, 329, 482

Hauser, M.G., Arendt, R. G., Kelsall, T., et al. 1998, ApJ, 508, 25

Holland, W. S., et al. 1999, MNRAS, 303, 659

Hughes, D., Serjeant, S., Dunlop, J., et al., 1998, Nature, 390, 257

Kawara, K., Sato, Y., Matsuhara, H., et al. 1998, A&A, 336, L9

Kawara, K., Matsuhara, H., Okuda, H., et al. 2004, A&A, 413, 843

Kessler, M.F., Steinz, J.A., Anderegg, M.E., et al. 1996, A&A, 315, L27

Kim, D.C. & Sanders, D.B., 1998, ApJS, 119, 41

Landolt, A. U. et al., 1992, AJ, 340, 436

Laurent, G. T., et al. 2005, ApJ, 623, 742

Lehmann, I., Hasinger, G., Schmidt, M., et al., 2001, A&A, 371, 833

Lemke, D., Klaas, U., Abolins, J., et al. 1996, A&A, 315, L64

Lockman, F.J., Jahoda, K., & McCammon, D., 1986, ApJ, 302, 432

Lonsdale, C. J., et al. 2003, PASP, 115, 897

Luppino,G., Metzger, M., Kaiser, N., et al. 1996, in ASP Conf. Ser. 88, Clusters, Lensing, and the Futere of the Universe, ed. V. Trimble & A. Reisenegger(San Francisco:ASP),229

Majewski, S.R., Kron, R.G., Koo, D.C., & Bershady, M.A., 1994, PASP, 1258

Mann, R.G., Oliver, S.J., Serjeant, S.B.G., et al., 1997, MNRAS, 289, 482

Mann, R.G., Oliver, S., Carball, R., et al., MNRAS, 332, 549

Matsuhara, H., Kawara, K., Sato, Y., et al., 2000, A&A, 361, 407

Mainieri, V., Bergeron, J., Hasinger, G., Lehmann, I., Rosati, P., Schmidt, M., Szokoly, G., & Della Ceca, R., 2002, A&A, 393, 425

Miyazaki, S., et al. 2002, PASJ, 54, 833

Monet, D., Bird, A., Canzian, B., et al., 1998, USNO-A2.0, (U.S. Naval Observatory)

Héraudeau, Ph., et al. 2004, MNRAS 354, 924

Patris, J., Dennefeld, M., Lagache, G, & Dole, H., 2003, A&A, 412, 349

Rodighiero, G,. Lari, C., Franceschini, A., Greganin, A., & Fadda, D., 2003, MNRAS, 343, 1155

Rodighiero, G,. & Franceschini, A., 2004, A&A, 419, L55

Rodighiero, G., Lari, C., Fadda, D., Franceschini, A., Elbaz, D., & Cesarsky, C. 2004, A&A, 427, 773

Rodighiero, G., Fadda, D., Franceschini, A, & Lari, C., 2005, MNRAS, 357, 449 Rodighiero, G,. Lari, C., Franceschini, A., Greganin, A., & Fadda,

Puget, J.L., Abergel,A., Bernard, J.P., et al., 1996, A&A, 308, L5

Puget, J.L., Lagache, G., Clements, D.L., 1999, A&A, 345, 29

Richards, E.A., 2000, ApJ, 533, 611

Rowan-Robinson, M., Broadhurst, T., Oliver, S.J., et al., 1991, Nature, 351, 719

Rowan-Robinson M. et al., 1997, MNRAS, 289, 490

Rutledge, E.R., Brunner, R.J., Prince, T.A., & Lonsdale, C., 2000, ApJS, 131, 335

Sanders, D. B. & Mirabel, I. F. 1996, ARA&A, 34, 749

Schmidt, M., 1968, ApJ, 151, 393

Scott, S. E., et al. 2002, MNRAS, 331, 817

Serjeant, S., et al. 2004, MNRAS, 355, 813

Stetson, P.B., 1987, PASP, 99, 191

Sheinis, A. I., Miller, J. S., Bolte, M., & Sutin, B. 2000, Proc. SPIE, 4008, 522

Smail, I., Ivison, R.J., & Blain, A.W., 1997, ApJ, 490, L5

Smith, H. E., Lonsdale, C. J., Lonsdale, C. J., & Diamond, P. J., 1998, ApJ, 493, L17

Soifer, B.T., Sanders, D.B., Mandore, B.F., et al., 1987, ApJ, 320, 238

Sutherland, W., & Saunders, W., 1992, MNRAS, 259, 413

Takeuchi, T.T., Ishii, T.T., Hirashita, H., et al., 2001, PASJ, 53, 37

Totani, T., Yoshii, Y., Iwamuro, F., Maihara, T., & Motohara, K., 2001, ApJL, 550, L137

Totani, T. & Takeuchi, T. T. 2002, ApJ, 570, 470

Theureau, G., Bottinelli, L., Coudeeau-Durand, N., et al., 1998, A&AS, 130, 333

Valdes, F., 1995, IRAF document "Guide to the HYDRA Reduction Task DOHYDRA" on the web: http://iraf.noao.edu

Veilleux & Osterbrock 1987, ApJS, 63, 295

Wolstencroft, R. D., Savage, A., Clowes, R. G., MacGillivray, H. T., Leggett, S. K., & Kalafi, M. 1986, MNRAS, 223, 279

Yun, M. S., Reddy, N. A., & Condon, J. J. 2001, ApJ, 554, 803

A. Comparison with Rodighiero et al.

Rodighiero et al. (2003) and Rodighiero & Franceschini (2004) have reduced our 90 μm data in the LHEX and LHNW fields, by using their own method, a parametric algorithm that fits the signal time history of each detector pixel. They then identified the singularities induced by cosmic ray impacts and by transient effects in the detectors and extract real sky sources. The numbers of their sources with signal-to-noise ratio S/N $>$ 3 are 36 and 28 in the LHEX and LHNW, respectively, while our catalogs consist of 116 and 107 sources having S/N $>$ 3(Kawara et al. 2004). Both catalogs are made with the different method. Thus the reason of this difference is expected to be in the reduction and source extracting methods, but is unclear.

In Table 6, their 15 LHEX and 11 LHNW sources have a counterpart within 30$''$ in our catalogs. Figure 16 compares the Rodighiero et al. flux with ours. One IRAS source, UGC 06009, is reported as ex003(577 $\pm$ 110 mJy) in Rodighiero et al. (2003), while we used this source for the flux calibration of the IRAS 100 μm measurement(1218 mJy). The difference of a factor of 2.1 between ours and Rodighiero et al. might be expected and the mean ratio of ours with those in Rodighiero et al. (2003) and Rodighiero & Franceschini (2004) is 1.8. As shown in Figure 16, there are some sources in our catalog having $\sim$100 mJy which show much fainter fluxes in theirs, and these sources could make the deviation of the flux ratio bigger.

Rodighiero et al. (2005) have done the identification work of their 36 90 μm sources(Rodighiero et al. 2003) in the LHEX field using the association with the shallow radio(de Ruiter et al. 1997) and 15 μm sources (Fadda et al. 2004; Rodighiero et al. 2004). 17 of them are identified with radio and 15 μm sources, all of which are optically identified. 14 of the 17 optically identified sources are found in our catalog(Kawara et al. 2004) and we made same optical identification in this paper. However only one(ex002/1EX100) of their 19 optically unidentified sources is found in Kawara et al. (2004) and is succeeded to identify in this work. It is unclear why most of their unidentified sources are not found in Kawara et al. (2004).

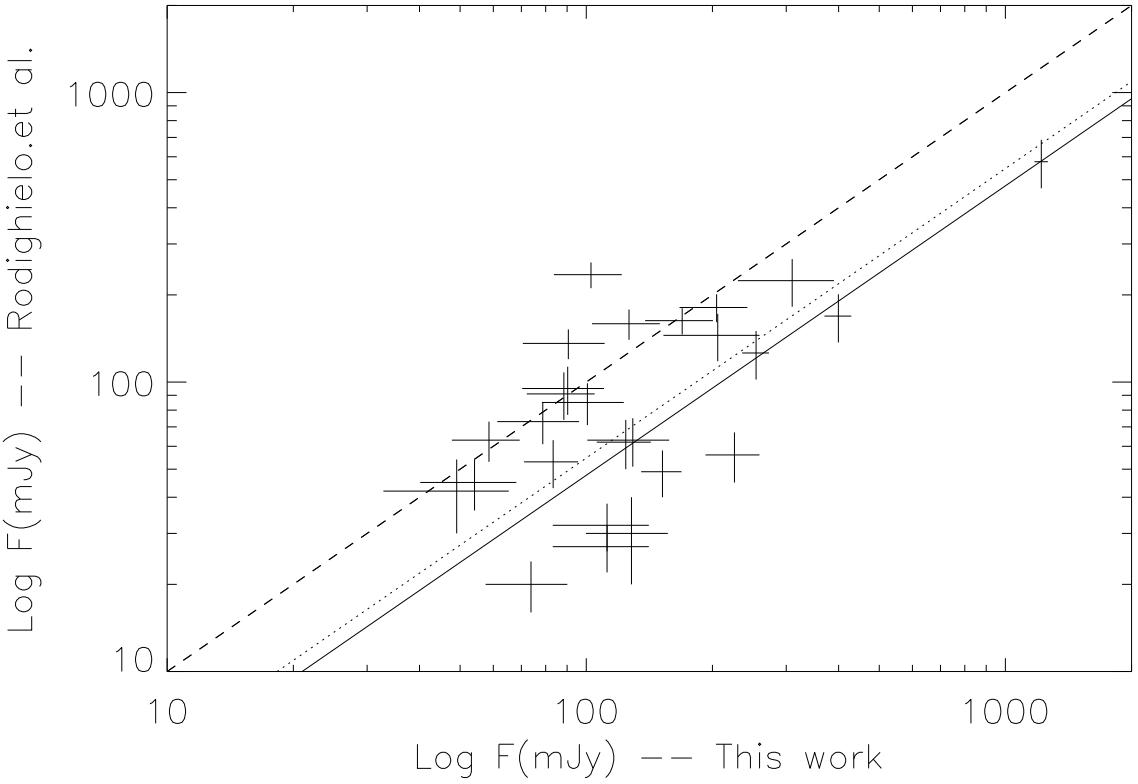

Fig. 16.— Comparison of our 90 μm fluxes with Rodighiero et al. (2003) and Rodighiero & Franceschini (2004). A solid line denote the ratio of 2.1 which comes from the flux difference of the IRAS source. The mean ratio of ours with those in Rodighiero et al. (2003) and Rodighiero & Franceschini (2004) is 1.8(dotted line) and a dashed line presents the ratio for 1.0.

Table 6. Identification with sources in Rodighiero et al.

Rodighiero et al.			Kawara et al.	
ID[a]	Name	Flux(mJy)	Name	Flux(mJy)[b]
ex001	LHJ105324+572921	95 ± 18	1EX026	90 ± 20
ex003[c]	LHJ105349+570716	577 ± 110	1EX023	1218 ± 44
ex004	LHJ105052+573507	224 ± 42	1EX041	310 ± 80
ex007	LHJ105300+570548	169 ± 32	1EX062	399 ± 29
ex008	LHJ105041+570708	126 ± 24	1EX048	254 ± 19
ex009	LHJ105254+570816	145 ± 27	1EX269	206 ± 53
ex012	LHJ105113+571415	91 ± 17	1EX081	88 ± 16
ex019	LHJ105318+572130	63 ± 12	1EX179	129 ± 29
ex020	LHJ105127+573524	49 ± 9	1EX076	152 ± 17
ex022[d]	LHJ105223+570159	32 ± 6	1EX148	112 ± 29
ex025	LHJ105206+570751	62 ± 12	1EX034	124 ± 18
ex027	LHJ105328+571404	53 ± 10	1EX125	83 ± 12
ex028[d]	LHJ105226+570222	27 ± 5	1EX148	112 ± 29
ex029	LHJ105132+572925	45 ± 9	1EX100	54 ± 14
ex036	LHJ105323+571451	20 ± 4	1EX126	74 ± 16
nw001	LHJ103521+580034	235 ± 24	1NW055	103 ± 19
nw002	LHJ103606+574715	163 ± 17	1NW023	169 ± 31
nw003	LHJ103604+574815	181 ± 20	1NW092	205 ± 38
nw006	LHJ103515+573330	136 ± 16	1NW025	91 ± 20
nw008	LHJ103318+574925	159 ± 19	1NW021	126 ± 23
nw011	LHJ103530+573139	73 ± 12	1NW043	79 ± 17
nw012	LHJ103409+572715	63 ± 10	1NW221	59 ± 11
nw016	LHJ103610+574330	85 ± 14	1NW022	101 ± 22
nw020	LHJ103249+573719	56 ± 11	1NW192	226 ± 33
nw026	LHJ103316+573136	30 ± 10	1NW031	128 ± 28
nw027	LHJ103327+574539	42 ± 12	1NW114	49 ± 16

[a]Source numbers with prefix ex or nw. The number follows the order of the appearance in their catalogs. The prefix, ex , presents sources in Rodighiero et al. (2003) and the prefix, nw, presents sources in Rodighiero & Franceschini (2004).

[b]These fluxes are corrected with Equ. (1).

[c]The IRAS source, UGC 06009, which is used for our flux calibration.

[d]ex022 and ex028 may be blending with each other.